The controls of pressure and water on highly anisotropic Mg Diffusion in Forsterite

Joshua M. R. Muir[*1,2], Feiwu Zhang[1] and Andrew M. Walker[2]

1) Institute of Geochemistry, Chinese Academy of Sciences, 99 West Lincheng Road, Guiyang, Guizhou 550081, China

2) School of Earth and Environment, University of Leeds, LS2 9JT, United Kingdom

*Corresponding author: j.m.r.muir@mail.gyig.ac.cn, a.walker@leeds.ac.uk, zhangfeiwu@mail.gyig.ac.cn

This is an Arvixpreprint which has not been peer reviewed. It has been submitted to Physics of the Earth and Planetary Interiors for review.

The controls of pressure and water on highly anisotropic Mg Diffusion in Forsterite

Joshua M. R. Muir[*1,2], Feiwu Zhang[1] and Andrew M. Walker[2]

3) Institute of Geochemistry, Chinese Academy of Sciences, 99 West Lincheng Road, Guiyang, Guizhou 550081, China

4) School of Earth and Environment, University of Leeds, LS2 9JT, United Kingdom

*Corresponding author: j.m.r.muir@mail.gyig.ac.cn, a.walker@leeds.ac.uk, zhangfeiwu@mail.gyig.ac.cn

Abstract

Mg diffusion is important for explaining many deformational properties in forsterite but its mechanism is unknown and so the effect of variables such as pressure or water content is difficult to constrain. Knowing the effect of water on Mg diffusion is important, as some parts of the upper mantle are very wet. In this study we used DFT to calculate the anhydrous and hydrous diffusion of Mg in forsterite. In anhydrous forsterite vacancy diffusion is highly anisotropic in the [001] direction and a combination of interstitial and vacancy diffusion is required to reproduce experimentally derived anisotropies. Interstitial diffusion is highly pressure dependant such that with increasing pressure the anisotropy of Mg diffusion decreases while temperature has little effect on this anisotropy. Hydrating the Mg vacancies causes small changes to the activation energy but a large increase in the attempt frequency of diffusion which causes a significant increase in the Mg diffusion rate. The main effect of water is to increase the number of vacancies which causes [001] Mg diffusion to increase by orders of magnitude compared to [010] and [100] diffusion. This effect is proportional to the proportion of water that forms $(2H)_{Mg}^{X}$ vacancies but even with the very small amounts of $(2H)_{Mg}^{X}$ that are required to match experimental diffusion rates [001] diffusion is over 4 orders of magnitude faster than [110] diffusion. Wet diffusion laws apply above <~5 wt. % ppm water. These results mean that in the absence of other factors except in the driest circumstances Mg diffusion in forsterite should be extremely anisotropic.

Keywords: Forsterite; Mg Diffusion; Water; DFT

1 Introduction

Diffusion of cations occupying the octahedral metal sites in olivine controls processes that are active in the Earth's crust and upper mantle, and which underpin a range of geophysical and geochemical techniques. In the upper mantle, where olivine with composition close to $(Mg_{0.9},Fe_{0.1})_2SiO_4$ is the dominant phase, the diffusivity of Mg is important in understanding electrical conductivity (Fei et al., 2018a, Yoshino et al., 2009, Yoshino et al., 2017, Schock et al., 1989) and could influence deformation even though Mg is a rapidly diffusing species as argued in Jaoul (1990). Anisotropic Mg diffusion could be an important factor in explaining the anisotropic conduction seen in high conductivity layers underneath young oceanic plates (Fei et al., 2018a) and, if Mg diffusion is important in forming olivine textures, could also help explain variety of textures that are formed by olivine under different conditions (Karato et al., 2008). Mg-Fe interdiffusion occurring in zoned phenocrysts from volcanic products is increasingly used as a petrological tool (diffusion chronometry) to understand the timescales of pre-eruptive processes operating in the days and weeks prior to eruption (e.g. Hartley et al. 2016 and Pankhurst et al. 2018). On a longer timescale diffusion-controlled exchange between Mg and Fe in olivine and spinel can be used to infer the post-crystallisation thermal history of ultramafic igneous bodies (Ozawa, 1984). Diffusion can also lead to magnesium and iron isotope fractionation (Teng et al., 2011). Our understanding and ability to model all of these processes relies on accurate determination of the Mg self-diffusion and M-site interdiffusion coefficients in olivine and thus this has been the focus of a range of experimental and computational studies reviewed by Chakraborty (2010). However, details of the atomic scale basis of Mg self-diffusion in olivine have thus far eluded a full explanation and this limits our ability to confidently make use of this data under the wide range of conditions where diffusion is important.

Previous studies have identified several key features of M site diffusion as well as questions that remain unanswered. Despite early uncertainty, it is clear that magnesium self diffusion is faster than the self diffusion of oxygen or silicon (for a review of this history see Chakraborty (2010)). Diffusion can be described by a basic equation $D^{sd} = D_0 \exp(-\frac{E_{act}}{k_B T})$ where D^{sd} is the rate of self diffusion, D_0 is

a preexponential factor, E_{act} is the activation energy, k_B is the boltzmann constant and T is the temperature. These two values can then be treated as fitting factors for experiments run at different temperatures. Recent experimental estimates of E_{act} and D_0 for tracer diffusion in forsterite are 1.68 $\times 10^{-7}$ m^2/s and 358±28 kJ/mol for Si, 1.68 $\times 10^{-4}$ m^2/s and 437±17 kJ/mol kJ/mol for O (Costa and Chakraborty, 2008) and 9.6×10^{-4} m^2/s and 400±60 kJ/mol (Chakraborty et al., 1994) or 4.0×10^{-9} m^2/s or 250±30 kJ/mol (Fei et al., 2018a) for Mg, all measured for diffusion in the [001] direction. If we consider one set of parameters- 1300 K and 0 GPa the diffusion rate D of Mg is $2.5x10^{-19}$ m^2/s in Fei *et al.* (2018a) or $2\text{-}6x10^{17}$ m^2/s in Chakraborty *et al.* 1994. There are thus significant experimental discrepancies in both the Mg self-diffusion rate and its response to temperature found in the literature. These discrepancies in Mg diffusion parameters are likely related to the effects of iron and water which can have large effects on these parameters (Fei et al., 2018a, Chakraborty, 2010) and to the experimental difficulties of performing self-diffusion experiments.

In detail, magnesium self-diffusivity is found to be mildly sensitive to pressure, to be anisotropic and to depend on the chemistry of the olivine crystal. There are some differences in experimental activation volumes 1-3.5 cm^3/mol (Chakraborty et al., 1994) or 4.0-4.6 cm^3/mol (Fei et al., 2018a) but in all cases these are small and so pressure has little effect on diffusion rates. Diffusion along [001] is faster than diffusion along [100], which is faster than diffusion along [010] (Chakraborty et al., 1994) though other studies found [010] diffusion to be faster than [100] (Andersson, 1987, Jollands et al., 2020). The inclusion of Fe on 10% of M sites reduces the activation energy and decreases the pre-exponential factor (to 275±25 kJ/mol and 5.6×10^{-8} m^2/s; Chakraborty et al., 1994).

Adding a small amount of water (in the form of OH^- groups incorporated within the olivine crystal) significantly enhances Mg diffusivity (Fei et al., 2018a). Hydrous diffusion has been described with the equation: $D_{Mg} = D_0(C_{H_2O})^r \exp(-\frac{E_{act}}{RT})$ with the effect of water described by an exponent r which has been found to be 1.2±0.2 for Mg tracer diffusion (Fei et al., 2018a) and to be ~1 for Fe-Mg interdiffusion (Wang et al., 2004). However, this water fugacity exponent is difficult to constrain by

experiment as diffusion increases with water content but decreases with pressure, which also increases water fugacity.

Although these experiments provide the critical data needed to model diffusion-controlled processes in olivine, several aspects of Mg diffusion remain enigmatic and some parameters have not been fully established. For example, the reason for the anisotropy of diffusion is not clear and the effect of pressure on this anisotropy has not been determined. Furthermore, the reason for the change in Mg diffusivity caused by the incorporation of water and the possible anisotropy of this effect has not been fully elucidated. Finally, recent experiments suggesting that Mg diffusivity depends on silica activity (Jollands et al., 2020) are hard to explain.

In order to understand diffusion in olivine it is necessary to consider the crystal structure, how this permits point defect mobility and the point defect chemistry that controls the defect concentration. Olivine's distorted hexagonal close packed oxygen sublattice contains two distinct octahedrally co-ordinated M sites: M1, on an inversion centre, and the less symmetric M2, which sits on a mirror plane. M1 sites share edges and form continuous chains along [001] while M2 sites are isolated from each other (sharing an edge with an M1 site and corners with other M1 and M2 sites). This structural anisotropy hits at a possible reason for the directional dependence of Mg diffusion in forsterite: vacancy mobility along chains of M1 could be high compared to more tortuous pathways between M1 and M2 sites. There are also two normally unoccupied octahedral sites in the olivine structure. Each is located half way between occupied M sites (and sharing faces with them) along [100]. We call the unoccupied octahedral site midway between two M1 sites I1, and the unoccupied octahedral site midway between two M2 sites I2. Attempts to explain experimentally determined magnesium diffusivity have largely focussed on the way that changing the physical or chemical conditions can alter the concentration of magnesium vacancies in olivine. Previously this has been done through examining the effect of charge balance conditions on vacancy Mg conditions when they are perturbed by iron and oxygen (Dohmen and Chakraborty, 2007) and by water (Fei et al., 2018a). Nevertheless,

whatever thermodynamic mechanism is proposed for introducing point defects, the atomic scale mechanism leading to their mobility is hard to determine by this approach.

Atomic scale simulation can be used to determine both what defects are present and how they can move in crystal structures. Simulations using interatomic potentials (Wright and Catlow, 1994, Walker et al., 2009, Jaoul et al., 1995), density functional theory (Brodholt, 1997) and QM/MM embedded clusters (Walker et al., 2009) suggest that vacancies on the M1 site are more stable than vacancies on the M2 site, that octahedrally coordinated magnesium interstitials are unstable on I1 but can form on I2, and that a split-interstitial structure (two magnesium ions in tetrahedral coordination located on opposite sides of the M1 site) is stable (Walker et al., 2009). The mobility of some of these defects has been studied using interatomic potentials (Bejina et al., 2009, Jaoul et al., 1995, Walker et al., 2009) where it was found that Mg vacancies are more mobile than Mg interstitials (Walker et al., 2009), that pressure has a limited effect on mobility along the M1 chain as was found in experiment (Jaoul et al., 1995, Bejina et al., 2009) and that vacancies overwhelmingly diffuse along the [001] M1 chain (Bejina et al., 2009). These studies have neglected important effects. First, interatomic potentials often behave poorly in unusual geometries and these are often formed during diffusion. Second, these studies consider only activation energies and not the time taken for diffusing point defects to overcome these barriers. And third, they do not convert their diffusion pathways into a macroscopic diffusion model and thus calculate rates of diffusion.

A further limitation of these studies is that they do not consider the effect of hydrogen on defects. Some theoretical work has been performed on the structure of hydrous defects in olivine. Early studies investigated the effect of hydrogen on defects using interatomic potentials (Wright and Catlow, 1994) but given how point defects alter the electronic structure of the crystal it has proven necessary to use electronic structure methods (Brodholt and Refson, 2000, Haiber et al., 1997, Braithwaite et al., 2002). More recent studies have investigated the interaction between hydrogen and trace elements such as titanium (Berry et al., 2007, Walker et al., 2007) or boron (Ingrin et al., 2014) or attempted to link atomic scale models of the structure of various hydrous defects with the results of infra spectroscopy

(Balan et al., 2011, Umemoto et al., 2011, Braithwaite et al., 2003). No structural model of the effects of hydrogen on Mg diffusion have been produced.

Thus there exists no detailed exploration of Mg diffusion in forsterite using electronic structure methods. In the following we make use of atomic scale simulation to understand the atomic scale mechanism of Mg diffusion in forsterite, determine the absolute diffusivity as a function of direction and how this is altered by pressure, and show how and why the presence of hydrogen alters this picture.

2 Methods

Compared to the timescale accessible to direct atomic scale simulation using molecular dynamics, point defect diffusion in minerals is usually slow. Methods available to simulate diffusion thus seek to describe diffusion by repeated rare events which can be studied in detail, and then combined in order to describe diffusion on a meaningful timescale. The rare events are typically hops of point defects between adjacent sites. For example, one of a number of atoms could migrate into a vacancy, effectively moving the vacancy and permitting diffusion via a vacancy mechanism, or an interstitial atom could move into one of a number of a different interstitial sites, permitting diffusion via an interstitial mechanism. Repeated occurrences of these hops leads to a random walk of the defect and bulk self-diffusion (Tilley, 1987). Our approach to simulating Mg diffusion in forsterite thus follows three steps. First, we make use of density functional theory to determine the structure and relative stability of a wide range of stable Mg point defects in forsterite. These models represent the ground state end-points of the hops leading to diffusion. Second, we probe the energy landscape that must by traversed by the defect during a hop. This provides us with the energy barrier that must be overcome for the hop to proceed and the structure of the transition state (the configuration with maximum energy on the minimum energy pathway between the start and end point). Boltzmann statistics tell us how likely it is for a point defect to have enough energy at a given temperature to overcome the energy barrier while simulation of the lattice vibrations of the ground and activated state allow us to calculate the frequency at which each hop is attempted. Third, we combine

information about multiple hops between different ground states using a kinetic Monte Carlo approach to access timescales long enough to observe the random walk and measure Mg diffusion in forsterite.

2.1 Defect calculations using density functional theory

All input parameters to our models of magnesium diffusion in forsterite are derived from atomic scale simulations. Specifically, we use a "planewave and pseudopotentials" approach (Payne et al., 1992), where density functional theory (DFT; Hohenberg and Kohn, 1964; Kohn and Sham, 1965) allows us to probe the energy of periodic boxes of simulated atoms. We use this to evaluate the ground state defect structures and energies, the structures and energies of the transition states, and the way atoms vibrate in these configurations. This approach allows us to calculate the hop activation energies and rates as a function of temperature and pressure, which are needed to simulate diffusion. These calculations were undertaken using version 16.11 of the CASTEP code (Clark et al., 2005), which makes use of a plane wave basis for valence electrons (a cut off energy of 1000 eV was used throughout) and pseudopotentials to describe core electrons (on-the-fly ultra soft pseudopotentials were used with 2s, 3p and 3s, 2s and 2p, 3s and 3p, and 1s in the valence for Mg, O, Si and H, respectively). The PBE (Perdew et al., 1996) exchange correlation functional (a revised GGA functional) was used and, Kohn-Sham wavefunctions were represented on a (4x4x4) k-point grid in reciprocal space (Monkhorst and Pack, 1976).

We created models of Mg vacancies by removing an Mg^{2+} ion from an M1 or M2 site in a (2x1x2) forsterite super cell, with cell parameters fixed to those of the defect free crystal. Interstitial defects were created by inserting an extra Mg^{2+} ion into potential interstitial sites in the structure. To account for atomic relaxation around the defects, the structure was then relaxed until the forces on all atoms were less than 0.01 eV/Å and an energy tolerance of 1×10^{-5} eV/atom was repeated. Repeating calculations with increased cutoffs changed the energy of the supercell by <0.1 meV/atom. The (2x1x2) supercell was used to ensure that there was roughly 10 Å between repeating vacancies in all directions, a distance we found to be sufficient to contain the important atomic relaxations.

Simulation cells containing vacancies or interstitials have a net charge and so the energy calculated by CASTEP includes a defect-defect interaction term between adjacent supercell which does not reflect our desired energy of a charged defect in an infinite medium. We can approximately correct for this interaction by assuming it is the energy of a periodic array of point charges in a uniform neutralising background charge. This was done using the method of Leslie and Gillan (1985), first used for forsterite by Brodholt (1997). To use this method the relative permittivity of the cell needs to be set - we used a value of 6.2 following Brodholt (1997).We repeated these calculations for a (4x2x4) supercell containing a Mg vacancy, and the vacancy energy changed by <0.01 eV, suggesting that our simulation cell size and energy corrections are sufficient for our needs.

Hydrous vacancies were created in a similar way, but we removed an Mg^{2+} ion and replaced it with 2 H^{+} ions. These H^{+} atoms were placed close to oxygen atoms around the vacancy and we searched for the most enthalpically stable arrangement. Hydrogens in a Mg vacancy bond to one of the 6 oxygen atoms that surround a Mg vacancy. There are 4 degenerate arrangements of 2 H bound to an O in the Mg vacancy and we sampled all of these. We note that these hydrous vacancies are charge neutral, so correction for spurious Columbic interactions was not required.

Knowing the energy of defects allows us to calculate their population with assumptions about their formation reactions. With hydrogen free defects the Mg Frenkel reaction ($Mg_{Mg}^{X} \rightarrow V_{Mg}'' + Mg_{I}^{\bullet\bullet}$) is the likely formation reaction for Mg vacancies (Dohmen and Chakraborty, 2007). This will be the source of defects in this work and the number of defects can be calculated from the knowledge of the defect energies of Mg vacancies and interstitials. For hydrated vacancies the situation is more complex as calculating the defect population requires knowing the free energy of water and all possible hydrated vacancies. Instead in this work we first assume that all water forms a vacancy such that the concentration of vacancies=concentration/fugacity of water and that water only forms hydrated Mg vacancies. While other types of hydrous defects are likely to be formed by water this simply acts as a scaling factor as the number of hydrated Mg vacancies should be roughly proportional to the concentration of water (Kohlstedt, 2006). Thus we have used the following equation:

$f_{H2O} \propto \gamma[(2H)_{Mg}^{X}]$ Equation 1

where f_{H2O} is the water fugacity and y is a constant that we have set to various values as discussed below.

Once ground state structures and energies for the various defects had been determined, we enumerated the possible hops (where a defect moves from location to location) and for each hop we determined the pathway and found the transition state structure and energy. We did this by using a constrained optimisation approach. We first determined an approximate path for the hop (for vacancy diffusion this consists of two vacancies with a Mg atom at a point between the vacancies, for interstitial diffusion the interstitial atom is located between stable interstitial sites). For each hop we tried multiple paths, but direct paths proved to have the lowest transition state energy in all cases. A path was defined by 10 images (with the Mg atom in different locations between the start and end point) and each image was relaxed with the migrating Mg fixed to the path by preventing its movement in one direction ([100] or [010] or [001]) with the fixed direction being that which has the longest distance along the path. This provides an energy profile along the path and a maximum energy point. We then searched for the transition state by moving along the path from the maximum energy point in 0.1 Å steps in both directions until a maximum was found. This is the candidate transition state. While this method may not definitely find the transition state our frequency calculations (below) typically returned a single imaginary eigenvalue of the dynamical matrix, as expected for a transition state. In the few cases, which were all for interstitial diffusion, where this was not the case the candidate transition state was found by manual adjustment based on visualising the eigenvectors of the imaginary phonon frequencies until a single imaginary eigenvalue was found. It turned out that this manual adjustment changed the activation energy of the hop by <0.01 eV suggesting that the constrained optimisation method is highly reliable for finding activation energies even if they are in complex parts of the energy hypersurface.

When determining the energy of the transition state for hydrated vacancies we assumed that hydrogen mobility is much higher than magnesium mobility (Novella et al., 2017) and so the hydrogen

atoms follow the vacancy adiabatically. The procedure followed for hydrated vacancies is that described above but with hydrogen placed in a range of different positions (and relaxed without constraints) for each image. Hydrogen ions were placed in the MO_6 octahedron at the start or end of the path leading to four configurations for each image. One of these has two hydrogen atoms in the "start" octahedron, one has two hydrogen atoms in the "end" octahedron and two configurations have one hydrogen in each octahedron. Each point of the path then has four energies and at each point the lowest energy is selected to construct the path and find the transition state. This procedure assumes that throughout the process of magnesium diffusion the hydrogen atoms can rearrange to minimise the energy. We also attempted placing H outside the two MO_6 octahedra, but this gave higher energies than the previous configurations. In this way our activation energies for diffusion in hydrous forsterite are the minimum possible barriers as they ignore any barriers to hydrogen migration.

We repeated the calculations described above at 0, 5 and 10 GPa and 1000, 1300 and 1600 K by setting the simulation cell dimensions to minimise the Gibbs free energy of the defect free cell. The effect of pressure is easily accounted for by adding the PV term to the internal energy of the system. The effect of temperature requires consideration of the thermal motion of the atoms. We include this effect by making use of lattice dynamics to evaluate the phonon frequencies and then use these to evaluate the vibrational entropy of the crystal. Phonon frequencies were determined using the finite displacement method of CASTEP with finite displacements of 0.01 bohr. All lattice dynamics calculations were performed for q=(0,0,0) for the supercell. While this calculation at a single q-point may introduce a significant sampling error all of our calculations involve comparisons between two very similar structures- the start/end point of a diffusion step and its transition state- and so the effect of sampling errors are likely to be small but this a limitation of the method. For lattice dynamics we tightened the convergence criteria on the forces and energy for the geometry optimisation to 0.001 eV/Å and 1×10^{-9} eV/atom, respectively- a few end points and transition states were sampled with 0.00075 and 5x10-^{10} eV/atom cuts off and the change in free energy caused by increased cutoffs was

<1 meV/atom. We determined the Gibbs free energy at a wide range of temperatures and at least 5 different volumes and then the energy at each volume with the following equations:

$$G(P,T,V) = U(V) + PV + E_{ZP}(V) - TS(T,V)$$ Equation 2

$$E_{ZP}(V) = \sum_{k,i} \frac{1}{2} \hbar \nu_{k,i}(V)$$ Equation 3

$$S(V) = -\sum_{k,i} \ln\left[1 - \exp\left(-\frac{\hbar \nu_{k,i}(V)}{k_B T}\right)\right] - \frac{1}{T}\sum_{k,i} \hbar \nu_{k,i}(V) \left[\exp\left(\frac{\hbar \nu_{k,i}(V)}{k_B T}\right) - 1\right]^{-1}$$ Equation 4

Where U(V) is the internal energy and $\nu_{k,i}(V)$ is the frequency of the phonon with wave vector *k* in the *i*-th band at volume V. At the pressure and temperature of interest the appropriate volume and energy was determined by fitting 2nd order polynomials across our volume range and minimising Equation 2. This method is quasi-harmonic as it ignores anharmonic effects beyond those caused by thermal expansion. Defected unit cells have different thermal expansions than perfect unit cells. This effect is not large but to simulate the dilute limit we used the thermal expansion of the perfect unit cell to determine the lattice parameters of the simulation cell used for the defect calculations presented here.

2.3 From defects to diffusion

The self-diffusion of a Mg by a vacancy mechanism can be represented by:

$$D_{Mg}^{sd-vac} = D_{Mg}^{Vac} N_{Vac}$$ Equation 5

Where D_{Mg}^{Vac} is the diffusion coefficient of Mg vacancies and N_{Vac} is the atomic fraction of Mg vacancies. As shown below, our atomic scale simulations suggest that diffusion of both interstitials and vacancies can be important for magnesium diffusion in pure forsterite. To account for this possibility, we use the assumption that vacancies and interstitials diffuse independently of each other, which means that the total self-diffusion of Mg in forsterite is given by:

$$D_{Mg}^{sd} = D_{Mg}^{Vac} N_{Vac} + D_{Mg}^{Int} N_{Int}$$ Equation 6.

For systems with simple geometry, the diffusion coefficients can be found analytically from the attempt frequency, the migration entropy, the activation energy and the crystal structure. For example, for a single hop the coefficient is given by (Poirier, 1985):

$$D_{Mg}^{Vac} = \frac{\alpha}{q_i} l^2 v exp\left(\frac{\Delta S_m}{k_B}\right) exp\left(-\frac{\Delta H_m}{k_B T}\right)$$ Equation 7

where α is a geometric prefactor to account for the degeneracy of the hop, q is a dimensionality constant (q = 2, 4 or 6 for 1, 2 or 3D diffusion), l is the length of the hop and the two exponential terms are the migration entropy and the migration enthalpy, respectively. This approach has been used to determine diffusion coefficients in a number of minerals including MgO, bridgmanite and post-perovskite (e.g. Vocaldo et al. 1995; Ammann et al. 2010). However, forsterite diffusion involves defects moving from one site to an inequivalent site via multiple different hops and so it becomes cumbersome to attempt to develop equations of this type. Instead we seek a numerical estimate of the diffusion coefficients by implementing a kinetic Monte-Carlo (KMC; Bortz et al. (1975)) simulation of the motion of a defect in a forsterite crystal.

For our KMC method we need to know the rate at which each Mg hop can occur. We used lattice dynamics to probe the vibration of atoms around the point defects in their ground state and transition state configurations which allows us to model the effect of temperature on point defect mobility. The rate, k, at which a defect hops from one location to another is given by:

$$k = v exp\left(\frac{\Delta S_m}{k_B}\right) exp\left(-\frac{\Delta H_m}{k_B T}\right)$$ Equation 8

where v is the attempt frequency (in Hz). The activation energy term was calculated from our constrained optimisation. In order to calculate the attempt frequency and activation entropy we used Vineyard theory (Vineyard, 1957) which is based on absolute rate theory. Both of the temperature-based factors (vibrational entropy and attempt frequency) are combined and found from the ratio of the calculated phonon frequencies:

$$v = \left(\frac{\prod_{j=1}^{N} \nu_j}{\prod_{j=1}^{N-1} \nu_{j'}}\right)$$ Equation 9

Where ν_j are the lattice frequencies of a defect in its stable starting position and ν_j' are the real lattice frequencies of the defect at the transition state of its hop. The latter has one imaginary frequency and so one less real frequency. As with the QHA this theory assumes a harmonic approximation since motions near the saddle point are treated with the theory of small oscillations. Once activation

energies and modified attempt frequencies have been calculated for each hop (and at each temperature and pressure of interest), we can calculate the rate of each hop and have all the atomic scale information in hand to evaluate the absolute diffusivity of magnesium in forsterite. These single hop parameters are then fed into our KMC algorithm.

First developed to allow the efficient simulation of Ising spin systems, KMC works by simulating the time evolution of a system between a collection of states, with transitions between states governed by a set of rules that includes a probability of that transition occurring in a given amount of time. Transitions between states are selected randomly (preserving the relative probability of each transition) and a clock is advanced by an appropriate amount after the state transition has been determined. This makes it useful for simulating complex transitions with many possible motions as the energetics of each motion can be calculated independently and then put collectively into a KMC algorithm. KMC has found a number of applications in extending atomic scale simulations to macroscopic behaviour, including the simulation of dislocation motion (Bulatov and Cai, 2006), chemical vapour deposition (Bagatur'yants et al., 2003) and point defect diffusion (Voter, 2007).

For our simulations, we followed the rejection-free residence time method of Voter (2007). A brief overview of this method shall be given with more detail in the Supplementary Information. For each state in the system (eg a vacancy on M1) we enumerate all possible hops from that state and then calculate the rate of each hop (k^i) (equation 8 using equation 9), the sum of the rates of all the hops k^{tot} and the probability of each hop occurring $p^i = \frac{k^i}{k^{tot}}$. We then use the weighted probability of each hop to randomly select a hop and a time for that hop to occur (escape time) using Equation 10:

$t^i = -\left(\frac{1}{k_{tot}}\right)\ln(r^2)$ Equation 10

Where r^2 is a random number between 0 and 1. At each stage of the calculation the randomly selected hop moves our defect a certain distance in a certain direction and the randomly determined escape time advances the clock. Thus as this algorithm progresses, we build a list of positions of the defect

as a function of time as it undergoes a random walk through the (infinite) crystal structure. We then can calculate the mean-squared displacement (MSD) of our defect (using the method of Leetmaa and Skorodumova (2015) as explained in the supplementary information) as a function of time. This can then be converted to diffusion using Equation 11:

$\langle x^2 \rangle = qDt$ Equation 11

2.4 Pressure correction

While DFT generally reliably reproduces pressure derivatives, the absolute pressures calculated by DFT are known to be systematically incorrect in that they are shifted in one direction. This arises as we use an approximation of the exchange-correlation term. As pressure differences are reliably reported (as the effects of the approximation largely cancel out) replication of experimental elasticities has been performed via simple correction schemes based on experimental volume and elasticity values. The most simple such method is a linear correction (Zhang et al., 2013), :

$P(V,T) = P^{DFT}(V,T) - P^{DFT}(V_0^{exp})$ Equation 12

Where the subscript 0 represents the value of a parameter at a reference volume. V_0^{exp} was set to 287.4 Å^3 taken from Isaak et al. (1989), Equation 12 gave a value of -4.95 GPa and so a basic correction would change our results at 0, 5 and 10 Gpa to -5, 0 and 5 Gpa respectively. Such methods have been benchmarked against experimental elasticities but it is unclear if such methods will work to correct defect energies and diffusion rates.

3 Results

3.1 Defect Energies and Concentrations

There are two sites for Mg vacancies in forsterite – the M1 and the M2 sites. M1 sites are strongly favoured over M2 sites in both anhydrous and hydrous cases (>0.9 eV in anhydrous and >0.6 eV in hydrous vacancies) with pressure increasing this favourability (Table 1). This preference for M1 over M2 vacancies agrees with previous calculations though there is some difference in the energy of this

preference (~1.9 eV with forcefield calculations (Walker et al., 2009) or ~0.8 eV using DFT (Brodholt, 1997)). In all cases hydrous vacancies will be those where $2H^+$ atoms have been added to an Mg vacancy creating a charge balanced "hydrous" vacancy that is $(2H)_{Mg}^{X}$ in Kroger-Vink notation. The most stable position has the $2H^+$ atoms residing inside the vacancy, each bound to an O (with an O-H bond length of ~1.00 Å**)** and on opposite sides of the vacancy. In the most stable M1 case both hydrogen atoms are bound to a O2 atoms, as also seen in Walker *et al.* (2009), whereas in the most stable M2 case one hydrogen is bound to an O1 and one to an O3 atom.

Fei *et al.* 2018a found an increase in Mg diffusion rate that was proportional to the amount of water that was present. They argued that this increase in diffusion was due to the formation of $(2H)_{Mg}^{X}$ vacancies in a ratio proportional to the amount of water in the system. There is some debate, however, about exactly where hydrogen resides in olivine and under what conditions these sites change (Matveev et al., 2001, Le Losq et al., 2019, Berry et al., 2005, Tollan et al., 2018, Lemaire et al., 2004, Mosenfelder et al., 2006, Mosenfelder et al., 2011, Padron-Navarta et al., 2014). The obvious mechanism for hydrogen enhanced Mg diffusion is through the creation of $(2H)_{Mg}^{X}$ and so that is what we shall examine but we acknowledge that the ratio of $(2H)_{Mg}^{X}$ to f_{H2O} is uncertain and is modified by many factors such as SiO_2 activity and crystal impurities. We will address this in the discussion section by looking at various values of γ in Equation 1.

We have also considered Mg interstitials. As with Walker et al. (2009) we found that the most stable position is a split interstitial at the M1 site with 2 Mg atoms displaced from the centre of this site in opposite [010] directions (shown in Figure S1). This arrangement is very stable with alternative arrangements of the Mg at this site all relaxing into this one. Even placing a Mg atom in an I1 site causes it to relax into this split interstitial arrangement. The other stable configuration is found by placing an additional Mg in the I2 site. The Mg interstitial in the I2 site has an octahedral coordination like the M1 and M2 and is thus geometrically similar to them. At 0 GPa the split M1 interstitial is slightly favoured over the I2 arrangement (~0.2 eV) but with increasing pressure the I2 configuration

is favoured (Table 1) as the split M1 arrangement is larger than the I2 arrangement. This is in contrast to QM-MM embedded cluster calculations where this difference was found to be very large with an M1 geometry favoured over an I2 geometry by ~4.4 eV (Walker et al., 2009). It is also in contrast with our own forcefield calculations where we were unable to stabilise an I2 arrangement as they relaxed into an M1 arrangement.

To calculation diffusion rates the concentration of vacancies is required (Equation 6). For intrinsic diffusion this come from minimising the free energy of the Frenkel reaction ($Mg_{Mg}^{X} \rightarrow V_{Mg}'' + Mg_{I}^{\bullet\bullet}$). When this reaction proceeds forward the positive enthalpy and the negative configurational entropy term both increase and at some concentration this provides a minimum energy. As the Mg interstitial is able to occupy two sites solving analytically for the free energy minimum is awkward. Instead we calculate the number of different arrangements of Mg vacancies and defects in the crystal considering all M1, M2, I1 and I2 sites and then calculate the probability of their occurrence and thus their configurational entropy. The steps for this are given in the supplementary information but the final result is that the equilibrium concentration in the intrinsic case comes from minimising Equation 13:

$\Delta G = \Delta E \times a - TS_{confa}$ Equation 13

Where a is a reaction vector for the Frenkel reaction. The results of this minimisation are given in Table 2. Pressure strongly decreases the number of defects (by increasing the positive formation energy) whereas temperature increases the number of defects (by increasing the negative configuration entropy).

In the hydrous case the number of hydrated vacancies $(2H)_{Mg}^{X}$ is dependant entirely on the value of γ in Equation 1. Table 2 shows the concentration of vacancies when γ=1. This would relate to a case where only $(2H)_{Mg}^{X}$ vacancies are formed in significant numbers. This would occur in perfect forsterite with no substitutional defects that could form water and in cases of high SiO2 activity

where $(4H)_{Si}^{X}$ vacancies are suppressed (Walker et al., 2007). Some other cases will be discussed in the discussion section. As can be seen, however, the number of hydrated vacancies that water can potentially create is many orders of magnitude larger than the number of intrinsic vacancies in the crystal and thus the chemistry of water in the crystal will be the dominant factor in all diffusion calculations.

3.2 Vacancy Hops

For Mg diffusion by vacancy hopping we found six different vacancy diffusion hops for which we calculated the geometries and energies of hopping. The hops that we have considered are shown and labelled in Figure 1 with their dimensions listed in Table S1 and described in the SI.

The activation energies and frequencies of these hops are presented in Table 3 and the barriers to diffusion are shown in Figure 2. Notably the A hop which is directly along the [001] direction has a substantially lower activation energy than all other M1 hops. The easiest hop from an M2 site is the C hop back to an M1 site. These two effects combine such that vacancies will diffuse easily along the [001] direction when in a M1 site and have difficulty escaping to an M2 site and will be converted quickly back to an M1 site when they do escape to an M2 site. The weighted probability of these hops is shown in Figure 2 and an alternative representative in Figure S2 demonstrating the overwhelming dominance of the A hop.

Comparing our activation energies to published values we find that our value for the favoured A hop of 0.75 eV is similar to literature values of 0.72 (Walker et al., 2009) and 0.62 eV (Bejina et al., 2009). Our other hops have some variation with those found in Walker et al. (2009)**.** To test whether this was an effect of simply using DFT as against using forcefields we recalculated our results using GULP with a TBH1 forcefield (Wright and Catlow, 1994) (Table S3, computational details in supplementary information). We find that generally DFT produces lower barriers than forcefield calculations but that the order of the hops is the same with both DFT and forcefield calculations. Crucially the activation energy of the easiest A hop (which controls the overall diffusion) is very similar with both methods

0.77/0.75 eV which means that both DFT and forcefield calculations return a very similar diffusivity for anhydrous vacancy diffusion.

Hydrating these vacancies has varied effects on the activation energies with it increasing some and decreasing others. The reason for these trends are considered more in the Supplementary Information but for the lowest energy A hop water increases the activation energy from 0.75 to 1.25 eV.

A large effect is seen on the temperature based factors (v-modified attempt frequency) of hopping. Most notably v of the easiest A hop increases by 4 orders of magnitude from an anhydrous value of 1.26E+13 Hz to 4.04E+17 Hz in the hydrous sample. The increased activation energy of hydrated vacancies slows down their hopping but the larger v speeds up their hopping. The increase in v is considerably larger and so hydrated vacancies hop faster than anhydrous vacancies. If we use equation 8 to consider the hopping rate of the fastest A hop anhydrous vacancies have a rate of 38.1 GHz while hydrous vacancies have a rate of 28,600 GHz (at 1500 K and 0 GPa), 3 orders of magnitude faster.

We also considered the effect of pressure on the activation energies of these vacancies. As shown in Table S4 and Table S5 going from 0 to 10 GPa makes negligible differences to the activation energy or v of any of the anhydrous or hydrous hops. The small differences seen are miniscule compared to the effect pressure has on the vacancy concentration as described above.

3.3 Mg interstitial hops

As Mg interstitials occupy M1 and I2 sites- the latter of which are simply shifted M2 sites- the geometry of interstitial hops are identical to those of vacancies. These hops are pictured and labelled in Figure 1 and their barriers in Figure 3 (and tabulated in Table S2) with their energies and frequencies in Table 3. The probability of any of the hop occuring is shown in Figure 3 and alternatively in Figure S3. These are again described in the supplementary information.

Interstitial hops I and J, which are between M1 and I2 sites, are the most favourable with energies <0.6 eV. In part this is because in the split M1 configuration one Mg at the M1 site is already close to

an I2 site. Pressure has a small effect on the attempt frequency (Table S5) but a relatively large effect on the activation energy of these hops (Table S6) with hop I becoming nearly barrierless by 10 GPa. Interstitial hops from the split M1 site have considerably lower attempt frequencies than the typical values between 1×10^{-12} and 1×10^{-13} Hz whereas hops from the I2 site show more typical attempt frequencies.

No hydrous interstitial mechanism was considered as one is not readily apparent. Mg vacancies have a formal charge of -2 which can thus be charge balanced by the addition of 2 H^+ ions with a formal charge of +1 each. Mg interstitials, on the other hand, have a formal charge of +2 and thus the addition of H^+ ions to a Mg interstitial will serve to destabilise it. Additionally creating a Mg vacancy produces a cavity in the structure which has room for 2 H^+ ions, no such space is created by adding an Mg interstitial which actually reduces the empty volume into which you could place a H^+ ion.

3.4 Diffusion

Using our KMC algorithm we can convert hops into diffusion rates. The diffusion coefficients for both vacancy and interstitial hopping are presented in Table 4 (these are listed at 5 and 10 GPa in Table S7 and S8). A few immediate points stand out. First both anhydrous and hydrous vacancy diffusion is highly anisotropic with [001] diffusion being orders of magnitude faster than [100] or [010]. This is an outcome of diffusion where the hop directly along [001] is ~0.75 eV easier than any other M1 hop. In the absence of any additional undiscovered hops/mechanisms this will always hold. Second the diffusion coefficients of hydrous vacancies are much higher due to their increased attempt frequencies and so even in the absence of additional vacancies, hydrous diffusion is orders of magnitude faster than anhydrous diffusion. Third interstitial diffusion is much more isotropic than vacancy diffusion due to the favourability of M1 to I2 hops which go in all three primary directions.

To calculate total diffusion of Mg in forsterite we added together the rates of Mg vacancy and interstitial diffusion. This assumes that Mg Frenkel pairs are not associated with each other. To test this assumption we calculated the binding energy of this pair by running separate simulations with isolated Mg vacancies and interstitials and then calculations with them adjacent in the same unit cell

and comparing the difference in enthalpy. We find that the binding energy is approximately -1.9 eV with a negative number indicating that bound defects are more stable than unbound defects. This is a large number but it is much smaller than the configurational energy gains of randomly scattering Mg vacancy and interstitial pairs for low concentrations. For the pairing energy to exceed this configuration entropy, the defect concentration would need to be above 1.2E-3 per unit cell at 1300 K, many orders of magnitude larger than the predicted vacancy concentrations (Table 2). Thus the Mg vacancy and interstitial pairs cannot be associated and can be modelled with individual diffusion.

Figure 4 compares our results at 5 GPa (which pressure corrects to roughly 0 GPa) to some experimental measures of Mg self-diffusion at 0 GPa. We only plotted results for experiments buffered with MgO because enstatite has been observed (in one case) to increase Mg diffusion rates by around 1 order of magnitude (Jollands 2020). As we can see our results for diffusion in the predominant [001] direction mostly match those of Chakraborty *et al.* 1994. In the [010] and [100] direction we match the results of Andersson 1989 and Chakraborty et al 1994 within experimental scatter. Other experiments have shown slightly faster diffusion than these results. The most straightforward explanation for increased diffusion rate is the presence of other defects in these crystals that have not been accounted for in our pure intrinsic diffusion systems. Other defects will increase the N_{vac} and N_{Int} terms in Equation 6 and thus increase the rate of diffusion. Our ability to replicate the results of Chakraborty *et al.* 1994 suggests that our model for diffusion in anhydrous forsterite accurately captures its diffusion. Critically if interstitials are not included in our model while [001] diffusion can be modelled accurately, [100] and [010] diffusion would be orders of magnitude slower than has been observed by experiment.

We next consider the effect of pressure. Figure 5 shows our anhydrous [001] diffusion rates (with values listed in Table S9) as a function of pressure. Notably we find a larger pressure derivative for intrinsic diffusion coefficients than has been seen in the literature (Chakraborty et al., 1994, Fei et al., 2018a). Our activation volumes are 6.69 cm^3/mol at 1000 K, 7.51 cm^3/mol at 1300 K and 7.84 cm^3/mol at 1600 K. The pressure dependence of diffusion is strongly controlled in our case by the

pressure dependence of defect concentration (Table 2) with little effect of the defect mobility (Table 4 compared with Table S7 and S8). Small changes to the formation energy of the Frenkel defect can have a strong effect on this dependence. If the number of defects is held constant across pressure then the calculated activation volumes are much smaller, ranging from -0.30 to 0.15 cm^3/mol. These lower activation volumes are of relevance for cases where pressure does not alter the number of vacancies. For example, in an extrinsic regime (where vacancies form to charge balance impurities) the vacancy concentration is not temperature or pressure dependent and only the direct effect of pressure on vacancy mobility is important. In a real crystal with few impurities there will be a balance between the number of vacancies formed intrinsically via Frenkel pairs and the number of vacancies associated with impurities. In such a case, the effective activation volume will fall between our high and low values.

4. Discussion

4.1 Anhydrous diffusion

One of the most notable features of our results is that Mg diffusion can be strongly anisotropic. Figure 6 shows the anisotropy of this diffusion as a function of pressure. We find that anisotropy decreases with pressure due to the increasing importance of interstitial diffusion, which is less anisotropic, with pressure while temperature has little effect on anisotropy. At 0 GPa we find that diffusion is strongly anisotropic. As both elasticity and diffusion rates are strong functions of unit cell volume Equation 12 likely represents a good approximate correction of our theoretical pressures and shall be used from here on. Thus at 1600 K at a corrected 0 GPa we find that the ratio of diffusivity in the [001] direction vs the [100] should be ~15 and the ratio of [001] to [010] diffusivity should be ~6. Experimental measures of these ratios have produced lower results with [001]:[100] having values of ~3 (Chakraborty et al., 1994), 3.5-7 (Jollands et al., 2020) 7-40 (Andersson, 1987) and [001]:[010] having values values of 4.5 (Chakraborty et al., 1994) 1.5-3.5 (Jollands et al., 2020) and 5-13 (Andersson, 1987). These experimental measurements were all at ambient pressures. Our values for this

anisotropy are somewhat larger but within the uncertainity of pressure values. It should be noted that while absolute pressures are less certain the calculated diffusion trends with pressure are much more accurate and thus there should always be a strong pressure dependant anisotropy of Mg diffusion in forsterite.

4.2 Hydrous diffusion

We now consider the effect of water on these diffusion rates**.** Water affects both the rate (Figure 7) and the anisotropy (Figure 8) of Mg diffusion in forsterite**.**

Considering first the diffusion rate (figure 7) water speeds up Mg diffusion primarily by creating large amounts of $(2H)_{Mg}^{X}$ vacancies with a much smaller secondary effect being that diffusion is sped up because $(2H)_{Mg}^{X}$ vacancines diffuse faster than V_{Mg}'' vacancies. Mg diffusion rates are thus highly dependent upon γ in Equation 1 because γ determines the concentration of $(2H)_{Mg}^{X}$ which in turn determines the diffusion rate (Equation 6).

To consider the value of γ we must consider the ways in which hydrogen can incorporate into the crystal. One possible way the reaction of water with forsterite can be rendered is R1:

$Mg_{Mg}^{\times} + H_2O + \frac{1}{2}SiO_2 = (2H)_{Mg}^{\times} + \frac{1}{2}Mg_2SiO_4$ R1

Other species in forsterite/olivine could react either with water directly or with $(2H)_{Mg}^{\times}$. If these reactions are more favoured then the concentration of $(2H)_{Mg}^{\times}$ would be proportionally reduced. One possibility that has been proposed in the literature is the formation of the "titano-clinohumite" defect through R2:

$(2H)_{Mg}^{X} + Ti_{Si}^{X} \rightarrow \{Ti_{Mg}^{\cdot\cdot}(2H)_{Si}''\}$ R2

which has been calculated to have a reaction energy of -169 kJ/mol (Walker et al., 2007). Such a favoured reaction would mean that Ti preferentially absorbs water over $(2H)_{Mg}^{X}$ and thus γ is strongly decreased when Ti is present. Another possibility is that $(2H)_{Mg}^{X}$ could react to form $(4H)_{Si}^{X}$. Such a reaction is strongly dependant on SiO_2 activity but is less favoured than R2 (Walker et al., 2007). While

all competing reactions for water will have an effect on γ the most energetically favourable reactions will have by far the largest effect and so identifying these reactions and establishing their thermodynamic favourability is critical to setting a value for γ. This is difficult to do both experimentally and theoretically because of how dependant γ will be upon crystal chemistry as well as pressure, temperature and water fugacity and this difficulty is demonstrated by the wide debate upon this problem in the literature as mentioned above. Instead in this work we shall consider some possible values for γ to demonstrate how changing this value changes the various properties of Mg diffusion.

The effect of γ on diffusion rate is shown in Figure 7 with three different values of γ showing three very different diffusion rates (with various additional values tabulated in Table S10 and S11). As a check upon whether our Mg diffusion rates are plausible we plot the experimentally measured values of Fei *et al.* (2018a). The first case comes where water solely produces $(2H)_{Mg}^{X}$ (γ=1). This produces a increase in the Mg diffusion rate by over 10 orders of magnitude which is an extremely large effect but such a situation only occurs in a perfect forsterite at high silica activity and so is unrepresentative of any real samples and is not reflective of the mantle. For the next case we consider the primary water sink in these crystals to be the reaction R2. The crystals in Fei *et al.* (2018a) contain 0.008 wt% TiO2 which is enough Ti to entirely segregate 8,000 wt% ppm water. For this case we took the energy of R2 as determined in Walker *et al.* 2007 and calculated how this would affect γ. Temperature, pressure and water concentration will have a big effect on the energy of R2 and thus on γ but we do not have the data to speculate on these effects and so we used a fixed value in order to obtain a rough estimate of this effect. The introduction of R2 drops the concentration of $(2H)_{Mg}^{X}$ and γ dramatically with γ having values of 2.67E-8 at 1000 K, 1.50E-6 at 1300 K and 1.84E-5 at 1600 K. At these first two considered values of γ water vacancies are sufficiently numerous that pressure does not have a major effect on Mg diffusion (assuming that the water fugacity is fixed independently of the pressure as we do here). For the third case we artificially set γ so that the rate of diffusion matches closely with the

values of Fei *et al.* (2018a). This requires a γ of 1.85E-9 at 1300 K. This could be achieved if R2 was favoured by an additional 0.75 eV at real conditions (such as by temperature or pressure) or if an alternative water sink that was around 2 eV more favourable than $(2H)_{Mg}^{X}$ was also present. At these low γ conditions pressure now becomes important to diffusion rates and their response to water as intrinsic defects and their strong dependence upon pressure become important. The results of Fei *et al.* (2018a) were determined at 8 GPa and so match closer to our high pressure values.

While Mg diffusion rates are heavily dependent on γ the concentration at which "wet" diffusion begins and the water fugacity exponent of Mg diffusion are not dependent on γ. The reason for both of these effects is the same and is because the concentration changes of $(2H)_{Mg}^{X}$ are so large relative to other factors in the system that all behaviours of diffusion versus water fugacity reflect how water fugacity changes the concentration of $(2H)_{Mg}^{X}$. In the case of the water fugacity exponent this was measured to be 1.00 for every system because Equation 1 as written has a water fugacity exponent of 1. Without considering configurational entropy the introduction of other competing water sink reactions- such as R2- will not change this exponent but this exponent will be changed by how other defects in the crystal affect the configurational entropy gains of forming $(2H)_{Mg}^{X}$. Typically this will be a small change and thus the water fugacity exponent of $(2H)_{Mg}^{X}$ reactions should not vary much from 1 as has been seen experimentally (Fei et al., 2018a). In all cases the diffusion regime changes from a "dry" regime to a "wet" regime <5 wt% ppm H_2O and generally below <1 wt% ppm.

Next we shall consider the anisotropy of hydrous diffusion. Hydrous diffusion is extremely anisotropic even when compared to anhydrous diffusion (Fig 8). The source of this anisotropy is clear as in hydrous diffusion anisotropic vacancy diffusion preponderates because water produces hydrous vacancies but not interstitials. While decreasing γ decreases this anisotropy even in our low γ case (which has a diffusion rate matching that of Fei *et al.* (2018a)) the anisotropy of the hydrous system is still over 3 orders of magnitude greater than the anisotropy of the anhydrous system and [001] diffusion is over 10,000 times faster than [110] diffusion at high pressure and water concentration.

This demonstrates that even very small amounts of hydrous diffusion drastically increases the anisotropy of Mg diffusion in olivine and to prevent this effect $(2H)_{Mg}^{X}$ concentrations would have to be reduced to a concentration where water would also not significantly change the diffusion rate of Mg diffusion.

Our main finding is thus that the anisotropy of Mg diffusion in forsterite is highly dependent on both pressure and water content, the latter of which could have major implications in the upper mantle.

4.3 Geophysical Implications

While the dependence of anisotropy on pressure is large this probably has little implication in the upper mantle. After applying pressure corrections a 0-10 GPa range in the upper mantle would be equivalent to ~5-15 GPa in our pressure scales. The largest changes in anisotropy come at the lowest pressures and so across the pressure range of the upper mantle changes in Mg diffusional anisotropy with depth will be typically an order of magnitude except at the coldest temperatures (1000 K) where this could reach 1.5 orders of magnitude. These changes are likely to too small to have any major effects on mantle rheology that change with depth.

Water dependant anisotropy is likely to be highly relevant. The upper mantle likely contains 50-200 ppm wt% water on average though some regions of it could be much richer (Hirschmann, 2006). If we consider such water concentrations in Figure 8 at pressures between 5-15 (in our uncorrected pressure scale) diffusion along [001] will be faster than diffusion along [110] by 6.5 to 12.5 orders of magnitude in the cases of γ=1 and by 1.5 to 5.5 (though generally ~3 to 4) orders of magnitude in our lowest considered γ case. Such a large anisotropic diffusion could have very large effects on the development of shape and crystal preferred orientations of olivine as well as potentially on the shape of grains and on the anisotropy of conduction in the wet upper mantle. Speculating on the exact nature of such an effect is difficult as the development of texture in olivine is complex and not fully

understood, see for example Jung (2017), and these results need to be replicated in experiments**.** When considering these processes, however, the possibly highly anisotropic nature of Mg diffusion should be considered.

It is important to stress that this increase in Mg diffusional anisotropy is tied to an increase in diffusion rate. It is possible to add water to forsterite in ways that won't increase the diffusion rate through creating defects that are not hydrated Mg vacancies and if water is added in such a fashion it won't change the anisotropy of Mg diffusion. It is only in situations where water increases the Mg diffusion rate that we expect a corresponding increase in anisotropy. Conversely, our model provides no way that water can increase the diffusion rate of Mg without also increasing the anisotropy of this diffusion.

We shall now consider ways in which water could increase the Mg diffusion rate, through increasing the population of hydrated Mg vacancies, without substantially increasing the Mg diffusional anisotropy in a real crystal. First it is possible that there is a mechanism of Mg diffusion in forsterite which is less anisotropic that we have not considered. Such a mechanism would have to coexist with some onerous requirements however. In this paper we have shown that the most conceptually simple mechanism of Mg diffusion in forsterite produces large anisotropy in wet conditions. This is a mechanism that exists and thus any alternative mechanism which is less anisotropic will have to diffuse Mg at a faster rate than this basic mechanism or it will be outcompeted. Our mechanism produces diffusion rates equivalent to experimental measurements for dry forsterite and thus a faster mechanism seems unlikely unless it is solely faster in the [100] and [010] directions. Such a mechanism would need to move Mg vacancies in the [100] and/or [010] directions with an activation energy that is roughly similar to the activation energy of the A hop in our mechanism ~0.8 eV. When you consider the large atoms that are in the way of any such movement it is difficult to imagine how such a mechanism could operate. Alternatively a macroscopic effect could mitigate the anisotropy of

microscopic diffusion. As one such possibility vacancies in forsterite have been shown to segregate strongly to dislocations (Skelton and Walker, 2018). In a crystal with a high concentration of dislocations this tendency could override the base diffusion mechanics. In extremely small crystals (<100 micron) grain boundary diffusion and diffusion in the boundary zone could be more important than bulk diffusion (Fei et al., 2018b). Outside of such macroscale effects it is difficult to recover hydrous Mg diffusion in forsterite that is isotropic.

Conclusions

We find that the anisotropy of Mg diffusion in forsterite is heavily dependent upon conditions with pressure weakly decreasing and water strongly increasing anisotropic diffusion in the [001] direction while temperature has little effect. To explain experimental diffusion rates in the [100] and [010] directions interstitial diffusion is required alongside Mg diffusion. We find a much larger water dependence of Mg diffusion than has been seen in experimental results which is likely due to water preferentially forming other defects beyond $(2H)_{Mg}^{X}$. Even when we account for such effects, however, hydrous Mg diffusion in forsterite remains extremely anisotropic. This diffusional anisotropy could affect many properties of olivine in places where it is sufficiently wet and rheological analyses that depend upon Mg diffusion, such as that performed in in Pankhurst *et al.* 2018, may need to be updated to allow anisotropy to vary with water content. If the extreme anisotropy predicted here holds in real samples then for example a paleo-hydrogmeter could be constructed for volcanic systems. It is essential to experimental test these predictions first, however, due to the extremely large anisotropy that is predicted.

Our methods here outline a conceptually simple model for Mg diffusion which can be expanded in straightforward ways. The next step is to consider how other components could affect this diffusion such as has been seen with enstatite (Jollands et al., 2020). This can performed in a similar method to how we have considered water. Additional components can either affect the number and balance of Mg vacancies and interstitials which will affect both diffusion rate and anisotropy of this diffusion

or they can affect the intrinsic diffusion of Mg vacancies and interstitials. The former effect can be considered by examining the energetics of defect forming reactions and how contaminants change these energetics- particularly through changing the configurational entropy balances- and the latter can be considered for contaminants that directly change Mg vacancies or interstitials by interacting with them.

Acknowledgments

Funding was provided by the National Environment Research Council as part of the Volatiles, Geodynamics and Solid Earth Controls on the Habitable Planet research programme (NE/M000044/1) and by National Natural Science Foundation of China (41773057). JM is highly thankful to Chinese Academy of Sciences (CAS) for PIFI.

Credit Author Statement: Joshua Muir Methodology Software Investigation Formal Analysis Writing-Original Draft Feiwu Zhang Funding Acquisition Andrew Walker Conceptualisation Methodology Writing- Review and Editing Supervision Resources Project Administration Funding Acquisition

Bibliography

AMMANN, M. W., BRODHOLT, J. P., WOOKEY, J. & DOBSON, D. P. 2010. First-principles constraints on diffusion in lower-mantle minerals and a weak D '' layer. *Nature,* 465**,** 462-465.

ANDERSSON, K. 1987. *Materietransport und Defektstrukturen in kristallinem Magnesiumorthosilicat bei höheren TemPeraturen.* Technischen Universität Clausthal.

ANDERSSON, K., BORCHARDT, G., SCHERRER, S. & WEBER, S. 1989. Self-diffusion in Mg_2SiO_4 (forsterite) at high temperature. *Fresenius Zeitschrift Fur Analytische Chemie,* 333**,** 383-385.

BAGATUR'YANTS, A. A., KORKIN, A. A., NOVOSELOV, K. P., SAVCHENKO, L. L. & UMANSKII, S. Y. 2003. Integrated approach to atomistic simulation of film deposition processes. *In:* CATLOW, C. R. A. & KOTOMIN, E. A. (eds.) *Computational Materials Science.* USA: IOS Press.

BALAN, E., INGRIN, J., DELATTRE, S., KOVACS, I. & BLANCHARD, M. 2011. Theoretical infrared spectrum of OH-defects in forsterite. *European Journal of Mineralogy,* 23**,** 285-292.

BEJINA, F., BLANCHARD, M., WRIGHT, K. & PRICE, G. D. 2009. A computer simulation study of the effect of pressure on Mg diffusion in forsterite. *Physics of the Earth and Planetary Interiors,* 172**,** 13-19.

BERRY, A. J., HERMANN, J., O'NEILL, H. S. C. & FORAN, G. J. 2005. Fingerprinting the water site in mantle olivine. *Geology,* 33**,** 869-872.

BERRY, A. J., WALKER, A. M., HERMANN, J., O'NEILL, H. S., FORAN, G. J. & GALE, J. D. 2007. Titanium substitution mechanisms in forsterite. *Chemical Geology,* 242**,** 176-186.

BORTZ, A. B., KALOS, M. H. & LEBOWITZ, J. L. 1975. NEW ALGORITHM FOR MONTE-CARLO SIMULATION OF ISING SPIN SYSTEMS. *Journal of Computational Physics,* 17**,** 10-18.

BRAITHWAITE, J. S., SUSHKO, P. V., WRIGHT, K. & CATLOW, C. R. A. 2002. Hydrogen defects in Forsterite: A test case for the embedded cluster method. *Journal of Chemical Physics,* 116**,** 2628-2635.

BRAITHWAITE, J. S., WRIGHT, K. & CATLOW, C. R. A. 2003. A theoretical study of the energetics and IR frequencies of hydroxyl defects in forsterite. *Journal of Geophysical Research-Solid Earth,* 108.

BRODHOLT, J. 1997. Ab initio calculations on point defects in forsterite (Mg2SiO4) and implications for diffusion and creep. *American Mineralogist,* 82**,** 1049-1053.

BRODHOLT, J. P. & REFSON, K. 2000. An ab initio study of hydrogen in forsterite and a possible mechanism for hydrolytic weakening. *Journal of Geophysical Research-Solid Earth,* 105**,** 18977-18982.

BULATOV, V. V. & CAI, W. 2006. *Computer Simulations of Dislocations,* UK, Oxford University Press.

CHAKRABORTY, S. 2010. Diffusion Coefficients in Olivine, Wadsleyite and Ringwoodite. *In:* ZHANG, Y. X. & CHERNIAK, D. J. (eds.) *Diffusion in Minerals and Melts.*

CHAKRABORTY, S., FARVER, J. R., YUND, R. A. & RUBIE, D. C. 1994. MG TRACER DIFFUSION IN SYNTHETIC FORSTERITE AND SAN-CARLOS OLIVINE AS A FUNCTION OF P, T AND FO2. *Physics and Chemistry of Minerals,* 21**,** 489-500.

CLARK, S. J., SEGALL, M. D., PICKARD, C. J., HASNIP, P. J., PROBERT, M. J., REFSON, K. & PAYNE, M. C. 2005. First principles methods using CASTEP. *Zeitschrift fuer Kristallographie,* 220**,** 567-570.

COSTA, F. & CHAKRABORTY, S. 2008. The effect of water on Si and O diffusion rates in olivine and implications for transport properties and processes in the upper mantle. *Physics of the Earth and Planetary Interiors,* 166**,** 11-29.

DOHMEN, R. & CHAKRABORTY, S. 2007. Fe-Mg diffusion in olivine II: point defect chemistry, change of diffusion mechanisms and a model for calculation of diffusion coefficients in natural olivine. *Physics and Chemistry of Minerals,* 34**,** 409-430.

FEI, H. Z., KOIZUMI, S., SAKAMOTO, N., HASHIGUCHI, M., YURIMOTO, H., MARQUARDT, K., MIYAJIMA, N. & KATSURA, T. 2018a. Mg lattice diffusion in iron-free olivine and implications to conductivity anomaly in the oceanic asthenosphere. *Earth and Planetary Science Letters,* 484**,** 204-212.

FEI, H. Z., KOIZUMI, S., SAKAMOTO, N., HASHIGUCHI, M., YURIMOTO, H., MARQUARDT, K., MIYAJIMA, N. & KATSURA, T. 2018b. Pressure, temperature, water content, and oxygen fugacity dependence of the Mg grain-boundary diffusion coefficient in forsterite. *American Mineralogist,* 103**,** 1354-1361.

HAIBER, M., BALLONE, P. & PARRINELLO, M. 1997. Structure and dynamics of protonated Mg2SiO4: An ab-initio molecular dynamics study. *American Mineralogist,* 82**,** 913-922.

HARTLEY, M. E., MORGAN, D. J., MACLENNAN, J., EDMONDS, M. & THORDARSON, T. 2016. Tracking timescales of short-term precursors to large basaltic fissure eruptions through Fe-Mg diffusion in olivine. *Earth and Planetary Science Letters,* 439**,** 58-70.

HIRSCHMANN, M. M. 2006. Water, melting, and the deep Earth H(2)O cycle. *Annual Review of Earth and Planetary Sciences.*

INGRIN, J., KOVACS, I., DELOULE, E., BALAN, E., BLANCHARD, M., KOHN, S. C. & HERMANN, J. 2014. Identification of hydrogen defects linked to boron substitution in synthetic forsterite and natural oliyine. *American Mineralogist,* 99**,** 2138-2141.

ISAAK, D. G., ANDERSON, O. L., GOTO, T. & SUZUKI, I. 1989. ELASTICITY OF SINGLE-CRYSTAL FORSTERITE MEASURED TO 1700-K. *Journal of Geophysical Research-Solid Earth and Planets,* 94**,** 5895-5906.

JAOUL, O. 1990. MULTICOMPONENT DIFFUSION AND CREEP IN OLIVINE. *Journal of Geophysical Research-Solid Earth and Planets,* 95**,** 17631-17642.

JAOUL, O., BERTRANALVAREZ, Y., LIEBERMANN, R. C. & PRICE, G. D. 1995. FE-MG INTERDIFFUSION IN OLIVINE UP TO 9 GPA AT T=600-900-DEGREES-C - EXPERIMENTAL-DATA AND COMPARISON WITH DEFECT CALCULATIONS. *Physics of the Earth and Planetary Interiors,* 89**,** 199-218.

JOLLANDS, M. C., ZHUKOVA, I. A., O'NEILL, H. S. & HERMANN, J. 2020. Mg diffusion in forsterite from 1250-1600 °C. *American Mineralogist***,** DOI: 10.2138/am-2020-7286.

JUNG, H. 2017. Crystal preferred orientations of olivine, orthopyroxene, serpentine, chlorite, and amphibole, and implications for seismic anisotropy in subduction zones: a review. *Geosciences Journal,* 21**,** 985-1011.

KARATO, S., JUNG, H., KATAYAMA, I. & SKEMER, P. 2008. Geodynamic significance of seismic anisotropy of the upper mantle: New insights from laboratory studies. *Annual Review of Earth and Planetary Sciences.*

KOHLSTEDT, D. L. 2006. The role of water in high-temperature rock deformation. *In:* KEPPLER, H. & SMYTH, J. R. (eds.) *Water in Nominally Anhydrous Minerals.* Chantilly: Mineralogical Soc Amer & Geochemical Soc.

LE LOSQ, C., JOLLANDS, M. C., TOLLAN, P. M. E., HAWKINS, R. & O'NEILL, H. S. C. 2019. Point defect populations of forsterite revealed by two-stage metastable hydroxylation experiments. *Contributions to Mineralogy and Petrology,* 174.

LEETMAA, M. & SKORODUMOVA, N. V. 2015. Mean square displacements with error estimates from non-equidistant time-step kinetic Monte Carlo simulations. *Computer Physics Communications,* 191**,** 119-124.

LEMAIRE, C., KOHN, S. C. & BROOKER, R. A. 2004. The effect of silica activity on the incorporation mechanisms of water in synthetic forsterite: a polarised infrared spectroscopic study. *Contributions to Mineralogy and Petrology,* 147**,** 48-57.

LESLIE, M. & GILLAN, M. J. 1985. THE ENERGY AND ELASTIC DIPOLE TENSOR OF DEFECTS IN IONIC-CRYSTALS CALCULATED BY THE SUPERCELL METHOD. *Journal of Physics C-Solid State Physics,* 18**,** 973-982.

MATVEEV, S., O'NEILL, H. S., BALLHAUS, C., TAYLOR, W. R. & GREEN, D. H. 2001. Effect of silica activity on OH-IR spectra of olivine: Implications for low-aSiO(2) mantle metasomatism. *Journal of Petrology,* 42**,** 721-729.

MOSENFELDER, J. L., DELIGNE, N. I., ASIMOW, P. D. & ROSSMAN, G. R. 2006. Hydrogen incorporation in olivine from 2-12 GPa. *American Mineralogist,* 91**,** 285-294.

MOSENFELDER, J. L., LE VOYER, M., ROSSMAN, G. R., GUAN, Y., BELL, D. R., ASIMOW, P. D. & EILER, J. M. 2011. Analysis of hydrogen in olivine by SIMS: Evaluation of standards and protocol. *American Mineralogist,* 96**,** 1725-1741.

NOVELLA, D., JACOBSEN, B., WEBER, P. K., TYBURCZY, J. A., RYERSON, F. J. & DU FRANE, W. L. 2017. Hydrogen self-diffusion in single crystal olivine and electrical conductivity of the Earth's mantle. *Scientific Reports,* 7**,** 10.

OZAWA, K. 1984. OLIVINE-SPINEL GEOSPEEDOMETRY - ANALYSIS OF DIFFUSION-CONTROLLED MG-FE-2+ EXCHANGE. *Geochimica Et Cosmochimica Acta,* 48**,** 2597-2611.

PADRON-NAVARTA, J. A., HERMANN, J. & O'NEILL, H. S. C. 2014. Site-specific hydrogen diffusion rates in forsterite. *Earth and Planetary Science Letters,* 392**,** 100-112.

PANKHURST, M. J., MORGAN, D. J., THORDARSON, T. & LOUGHLIN, S. C. 2018. Magmatic crystal records in time, space, and process, causatively linked with volcanic unrest. *Earth and Planetary Science Letters,* 493**,** 231-241.

PAYNE, M. C., TETER, M. P., ALLAN, D. C., ARIAS, T. A. & JOANNOPOULOS, J. D. 1992. ITERATIVE MINIMIZATION TECHNIQUES FOR ABINITIO TOTAL-ENERGY CALCULATIONS - MOLECULAR-DYNAMICS AND CONJUGATE GRADIENTS. *Reviews of Modern Physics,* 64**,** 1045-1097.

POIRIER, J. P. 1985. *Creep in Crystals,* UK, Cambridge University Press.

SCHOCK, R. N., DUBA, A. G. & SHANKLAND, T. J. 1989. ELECTRICAL-CONDUCTION IN OLIVINE. *Journal of Geophysical Research-Solid Earth and Planets,* 94**,** 5829-5839.

SKELTON, R. & WALKER, A. M. 2018. Atomistic Simulations of Mg Vacancy Segregation to Dislocation Cores in Forsterite. *EarthArXiv***,** DOI:10.31223/osf.io/shwut

TENG, F. Z., DAUPHAS, N., HELZ, R. T., GAO, S. & HUANG, S. C. 2011. Diffusion-driven magnesium and iron isotope fractionation in Hawaiian olivine. *Earth and Planetary Science Letters,* 308**,** 317-324.

TILLEY, R. J. D. 1987. *Defect Crystal chemistry and its applications,* United States, Kluwer Academic Publishers.

TOLLAN, P. M. E., O'NEILL, H. S. C. & HERMANN, J. 2018. The role of trace elements in controlling H incorporation in San Carlos olivine. *Contributions to Mineralogy and Petrology,* 173.

UMEMOTO, K., WENTZCOVITCH, R. M., HIRSCHMANN, M. M., KOHLSTEDT, D. L. & WITHERS, A. C. 2011. A first-principles investigation of hydrous defects and IR frequencies in forsterite: The case for Si vacancies. *American Mineralogist,* 96**,** 1475-1479.

VINEYARD, G. H. 1957. FREQUENCY FACTORS AND ISOTOPE EFFECTS IN SOLID STATE RATE PROCESSES. *Journal of Physics and Chemistry of Solids,* 3**,** 121-127.

VOCADLO, L., WALL, A., PARKER, S. C. & PRICE, G. D. 1995. ABSOLUTE IONIC-DIFFUSION IN MGO - COMPUTER CALCULATIONS VIA LATTICE-DYNAMICS. *Physics of the Earth and Planetary Interiors,* 88**,** 193-210.

VOTER, A. F. 2007. INTRODUCTION TO THE KINETIC MONTE CARLO METHOD. *In:* SICKAFUS, K. E., KOTOMIN, E. A. & UBERUAGA, B. P. (eds.) *Radiation Effects in Solids.* Dordrecht: Springer.

WALKER, A. M., HERMANN, J., BERRY, A. J. & O'NEILL, H. S. 2007. Three water sites in upper mantle olivine and the role of titanium in the water weakening mechanism. *Journal of Geophysical Research-Solid Earth,* 112**,** 12.

WALKER, A. M., WOODLEY, S. M., SLATER, B. & WRIGHT, K. 2009. A computational study of magnesium point defects and diffusion in forsterite. *Physics of the Earth and Planetary Interiors,* 172**,** 20-27.

WANG, Z. Y., HIRAGA, T. & KOHLSTEDT, D. L. 2004. Effect of H+ on Fe-Mg interdiffusion in olivine, (Fe,Mg)(2)SiO4. *Applied Physics Letters,* 85**,** 209-211.

WRIGHT, K. & CATLOW, C. R. A. 1994. A computer simulation study of (OH) defects in olivine. *Physics and Chemistry of Minerals,* 20**,** 515-518.

YOSHINO, T., MATSUZAKI, T., SHATSKIY, A. & KATSURA, T. 2009. The effect of water on the electrical conductivity of olivine aggregates and its implications for the electrical structure of the upper mantle. *Earth and Planetary Science Letters,* 288**,** 291-300.

YOSHINO, T., ZHANG, B. H., RHYMER, B., ZHAO, C. C. & FEI, H. Z. 2017. Pressure dependence of electrical conductivity in forsterite. *Journal of Geophysical Research-Solid Earth,* 122**,** 158-171.

ZHANG, Z., STIXRUDE, L. & BRODHOLT, J. 2013. Elastic properties of $MgSiO_3$-perovskite under lower mantle conditions and the composition of the deep Earth. *Earth and Planetary Science Letters,* 379**,** 1-12.

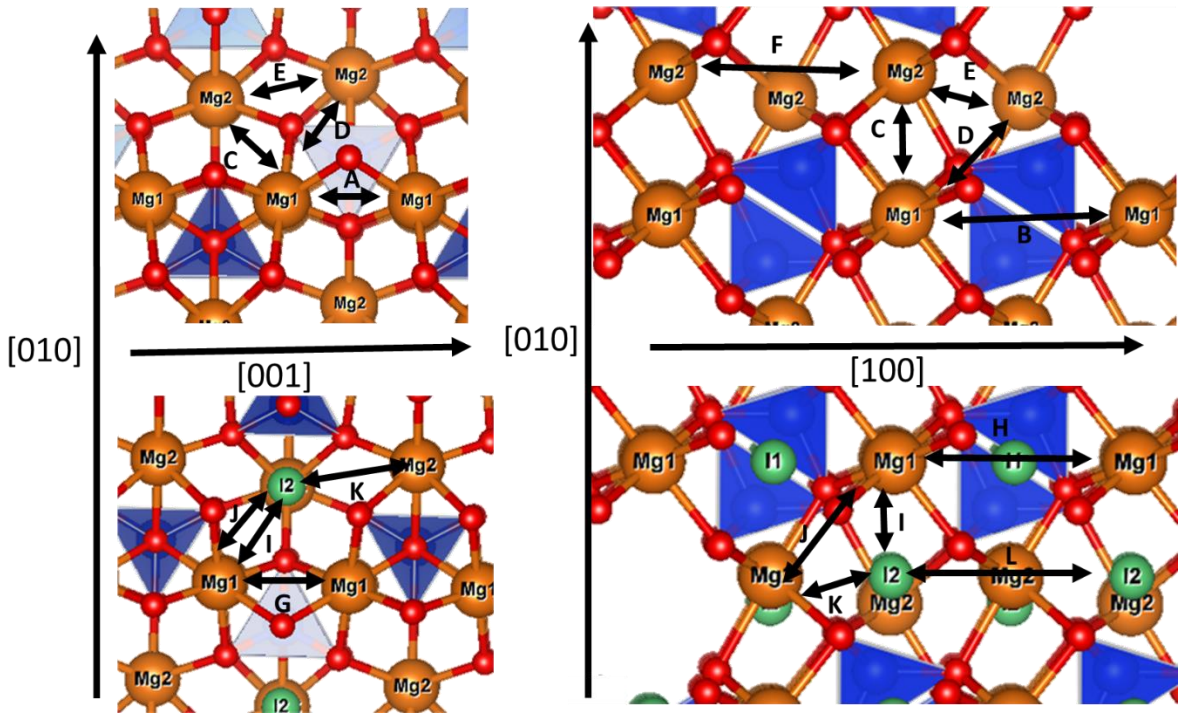

Figure 1:

Diagram of possible vacancy (top) and interstitial (bottom) hops. Vacancies hop between Mg1 and Mg2 sites, interstitials hop between I2 and M1 sites. The absolute distances of these hops are listed in Table S1 and S4. Mg atoms are brown, Si atoms are blue with their tetrahedrons highlighted, oxygen atoms are red, octahedral holes (only shown for interstitial hops) are green. The dimensions of these hops are given in Table S1 and Table S2.

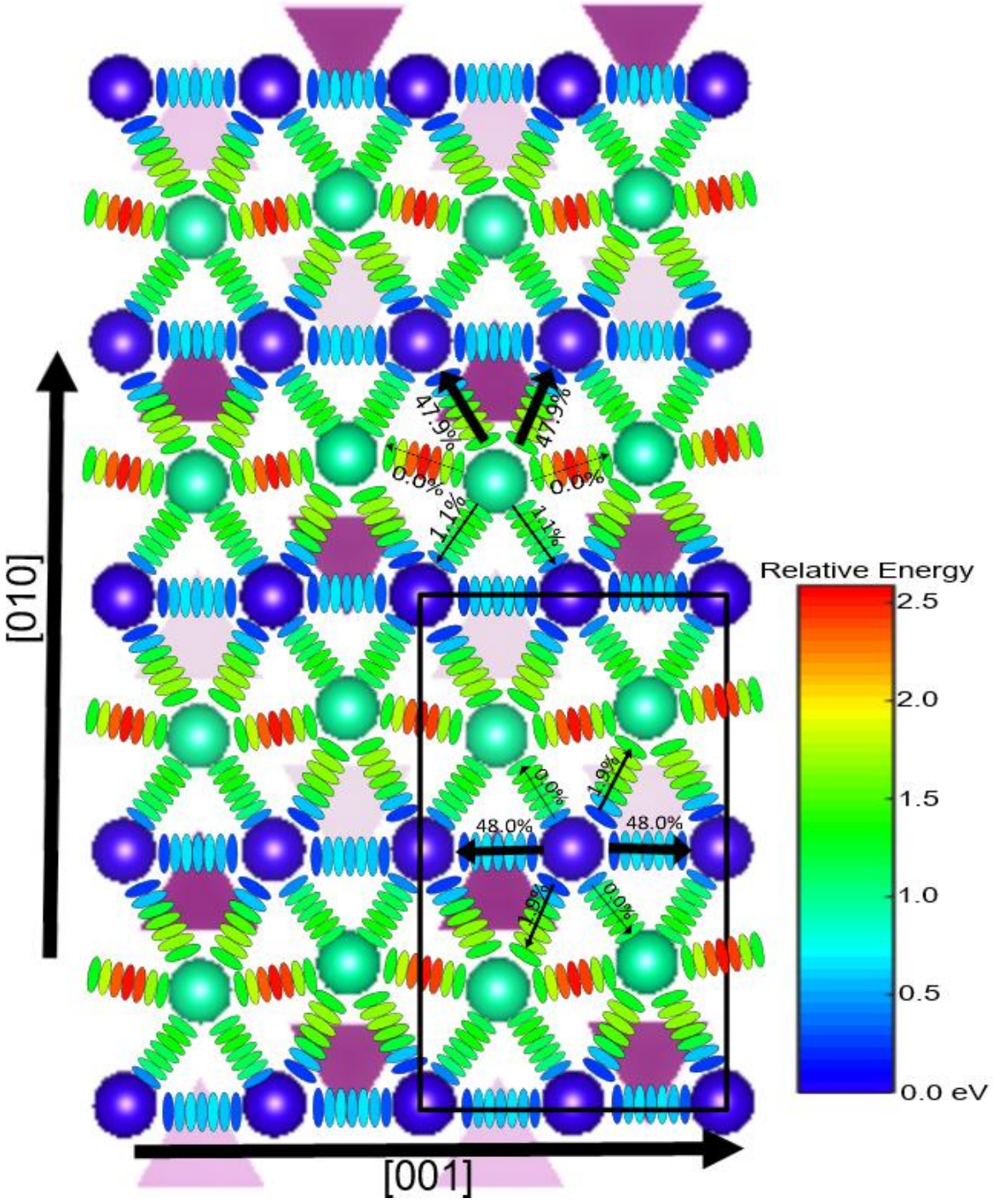

Figure 2: Plot of the activation energy barriers to Mg vacancy hopping in anhydrous forsterite. The energy of a vacancy is plotted at M1 (blue) (defined as 0 eV) and M2 (green) sites and at 7 points in-between each site with both the site and the intermediate points plotted with the same relative energy bar as shown. Many more intermediate points were used to determine the activation energy maximum (see text for details). Hops in the [100] direction (hops B and F) are not shown but both of these hops have activation energies higher than all the hops pictured here. The black box represents a forsterite unit cell. For a sample M1 and an M2 site we have shown the main hops with a percentage likelihood of selecting this hop that was determined at 1300 K and 0 Gpa.

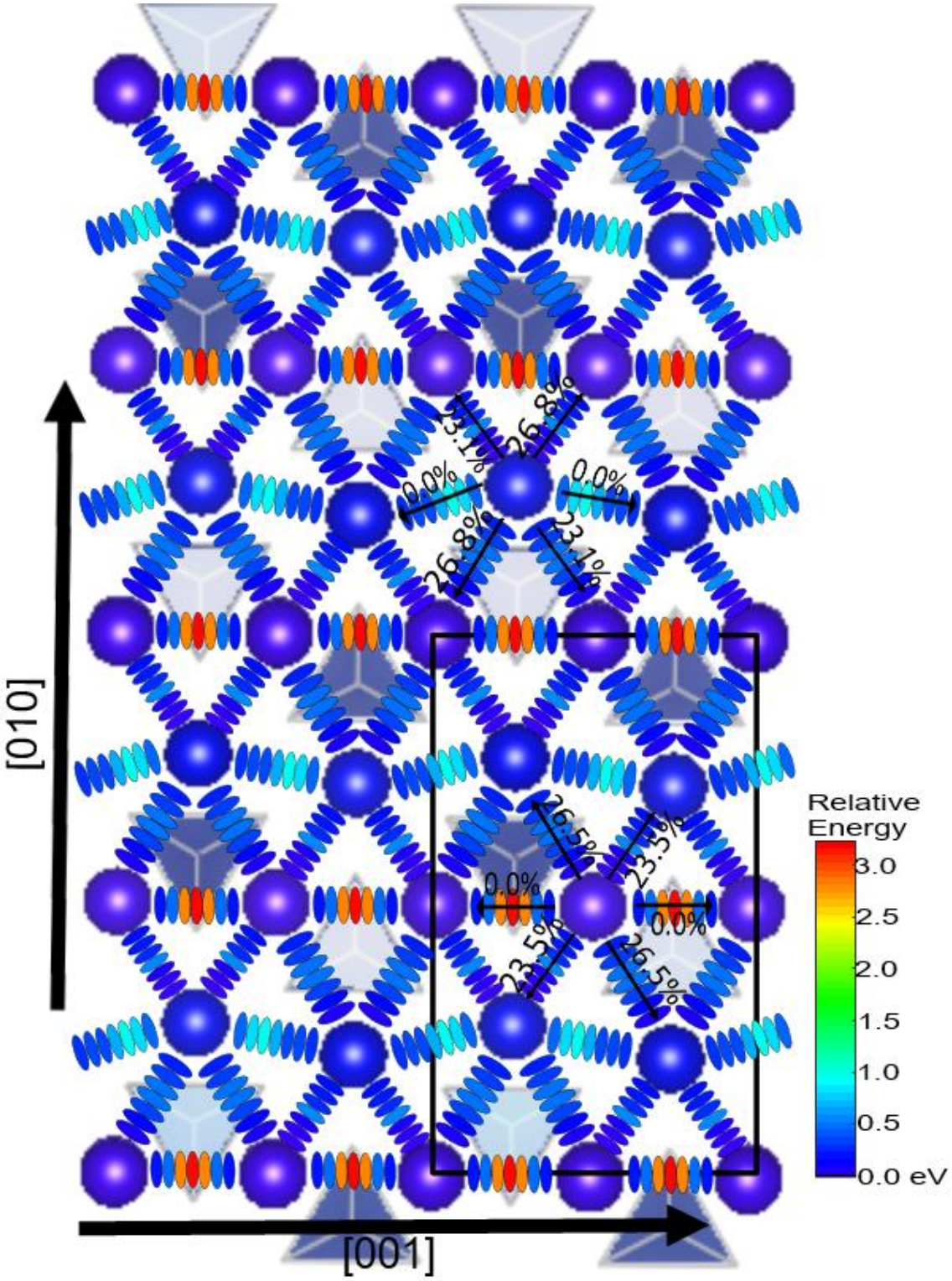

Figure 3: As Figure 2 but for interstitial hops between M1 and I2 sites with the M1 sites being defined as 0 eV. The layer closer to the bottom of the graph are M1 and then I2 and M1 layers alternate going up the page. These sites are much closer in energy than the M1 and M2 sites for vacancy migration. Again hops along the [100] axis (H and L) are not shown but are very high in energy. With this projection I and I* and J and J* hops are on top of each other (as they are only varied along the [100] direction) but we have pictured the lower energy paths (I and J respectively).

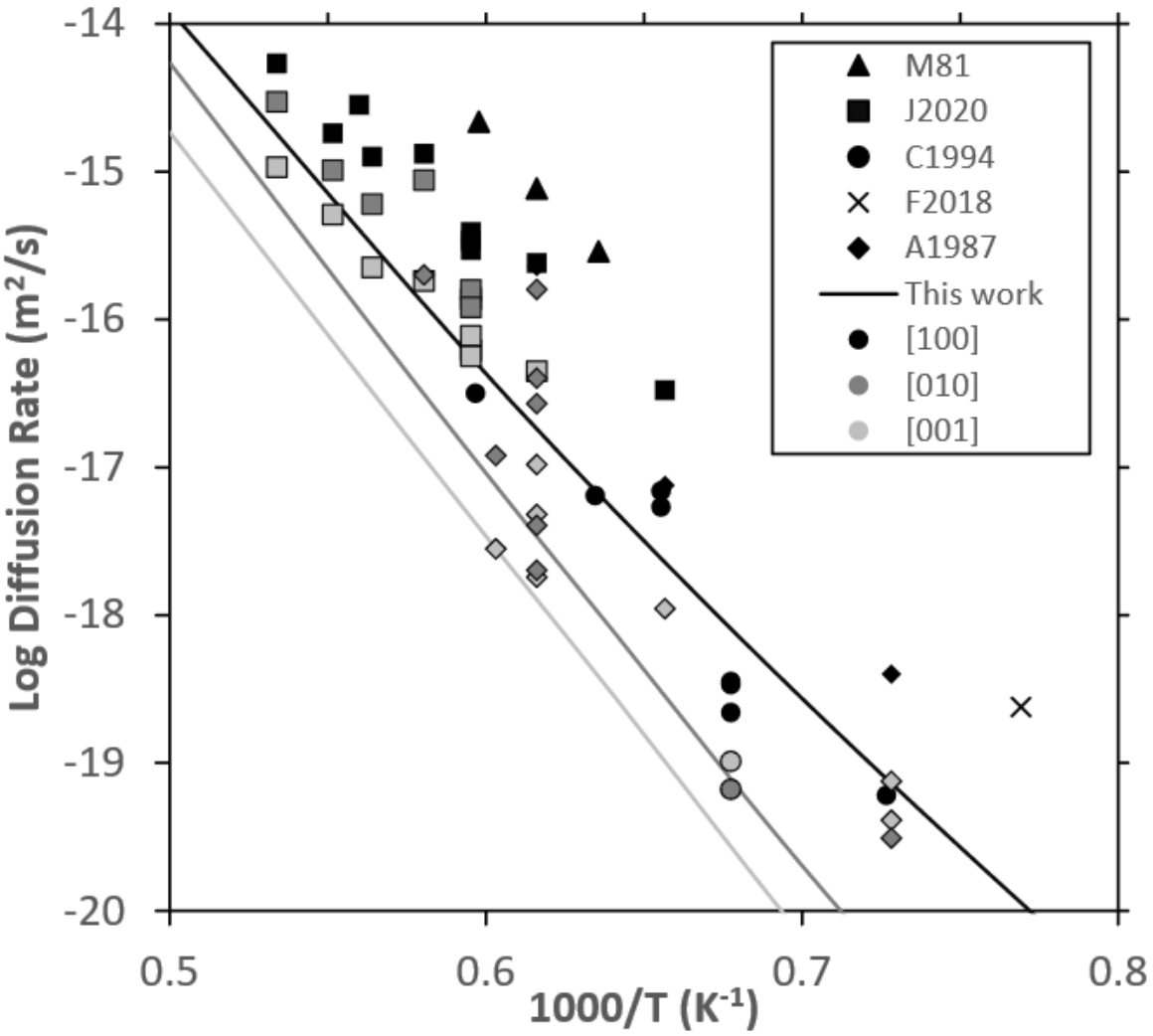

Fig 4: Plot of experimental Mg self diffusion rates in Mgo-buffered forsterite at 0 GPa alongside our predicted rates at 5 GPa (with a pressure correction of 5 GPa this equals 0 GPa). Rates have been separated by diffusion direction (shade- black= [001], dark grey= [010], light grey= [100]) and by the work they come from (symbol-see below). The lines represent our own calculations. In this collection we have excluded work in olivine and work buffered by enstatite. The mark for Fei *et al.* (2018a) was determined by our own extrapolation of the high temperature data across different pressures, all other points were as measured in the experiment. References are Morioka *et al.* 1981 triangles, Jollands *et al.* 2020 squares, Chakraborty *et al.* 1994 circles, Fei *et al.* (2018a) cross, , Andersson *et al.* 1987 diamonds.

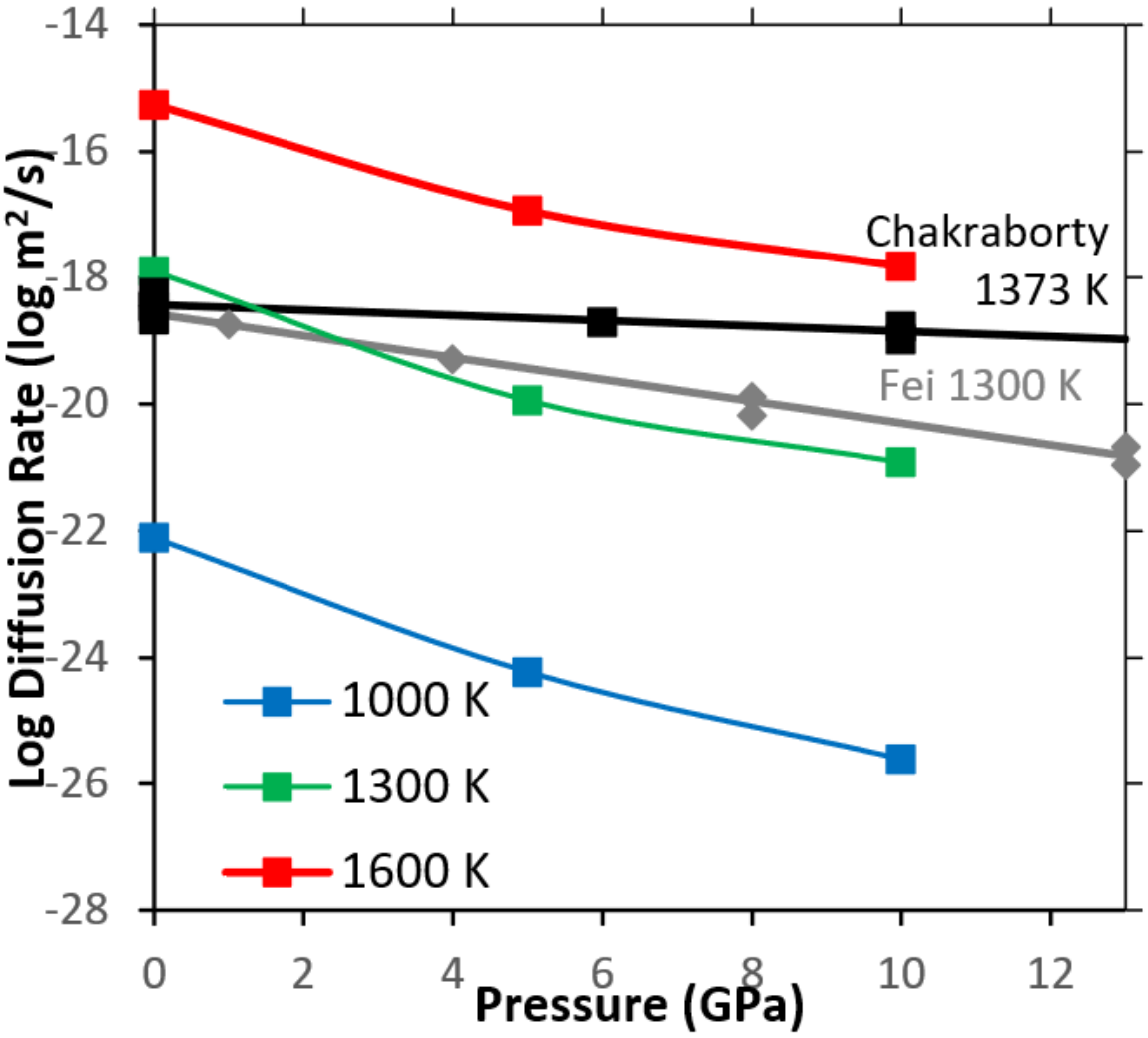

Figure 5: [001] Mg diffusion rates in perfect forsterite as a function of pressure at fixed temperatures (blue=1000 K, green=1300, red=1600) compared to results from Chakraborty *et al.* (1994) and Fei *et al.* (2018a). In both cases experimental data points are plotted and then a line is constructed using activation volumes of 1.1 cm^3/mol for Fei *et al.* (1994) and 4.3 cm^3/mol for Fei *et al.* (2018a). The results from Chakraborty *et al.* (1994) are those buffered by periclase with an f_{O_2} of 10^{-12}. In these results a higher activation volume (~3.4) was determined in air. The oxygen fugacity of Fei *et al.* (2018a) is unknown due to the complicated presence of water. For corrected pressure the results from this study should be shifted 5 GPa to the left.

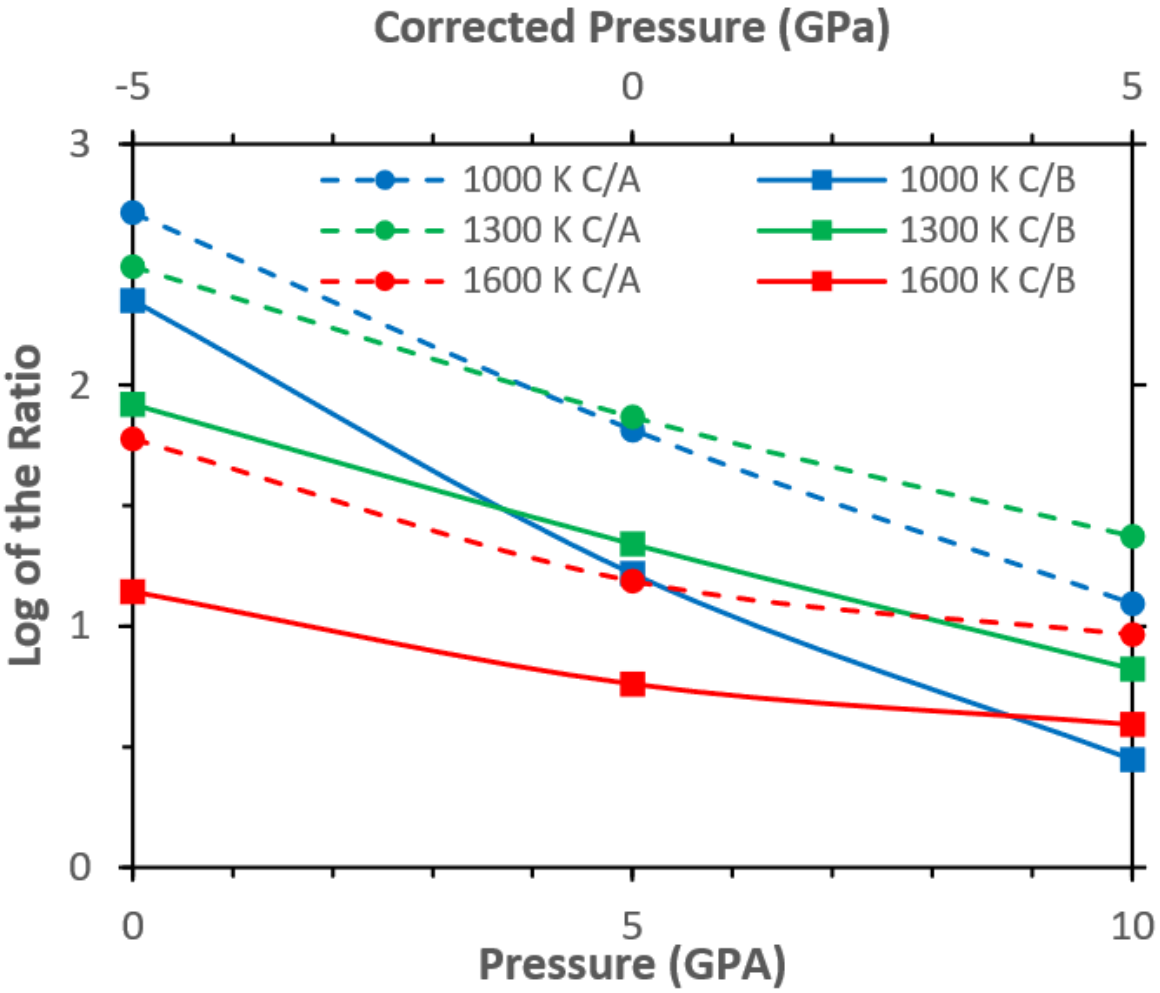

Figure 6: Log of the ratios of [001]/[100] (dotted lines, circles) and [001]/[010] Mg diffusion (solid line, squares) in perfect olivine as a function of pressure at different temperatures (blue 1000 K, green 1300, red 1600). Two pressure scales are shown, the pressure scale from DFT and one shifted by 5 GPa to represent a simple pressure correction.

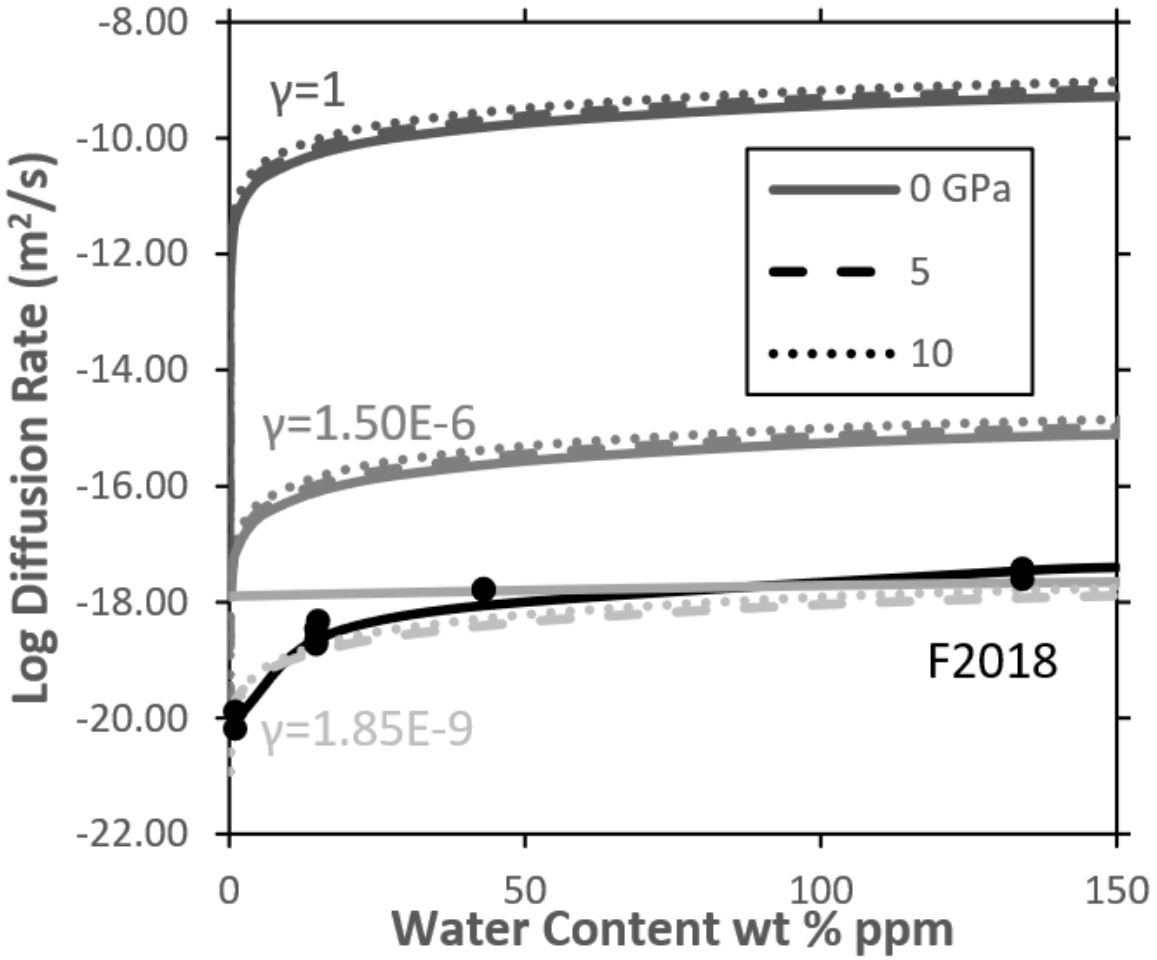

Figure 7: Plot of the Mg diffusion rate in forsterite as a function of water content at 1300 K (1000 and 1600 are plotted in Figure S4 and S5 but the effect of water and γ is very similar**).** Different pressures are shown with different line types (solid=0, dashed=5, dotted=10 GPa, all uncorrected). Different values for γ (Equation 1 and discussed more in text) are shown with different shades**.** The black line shows data points from Fei *et al.*(2018a) for 1300 K measurements alongside a fit using their water exponent of 1.2.

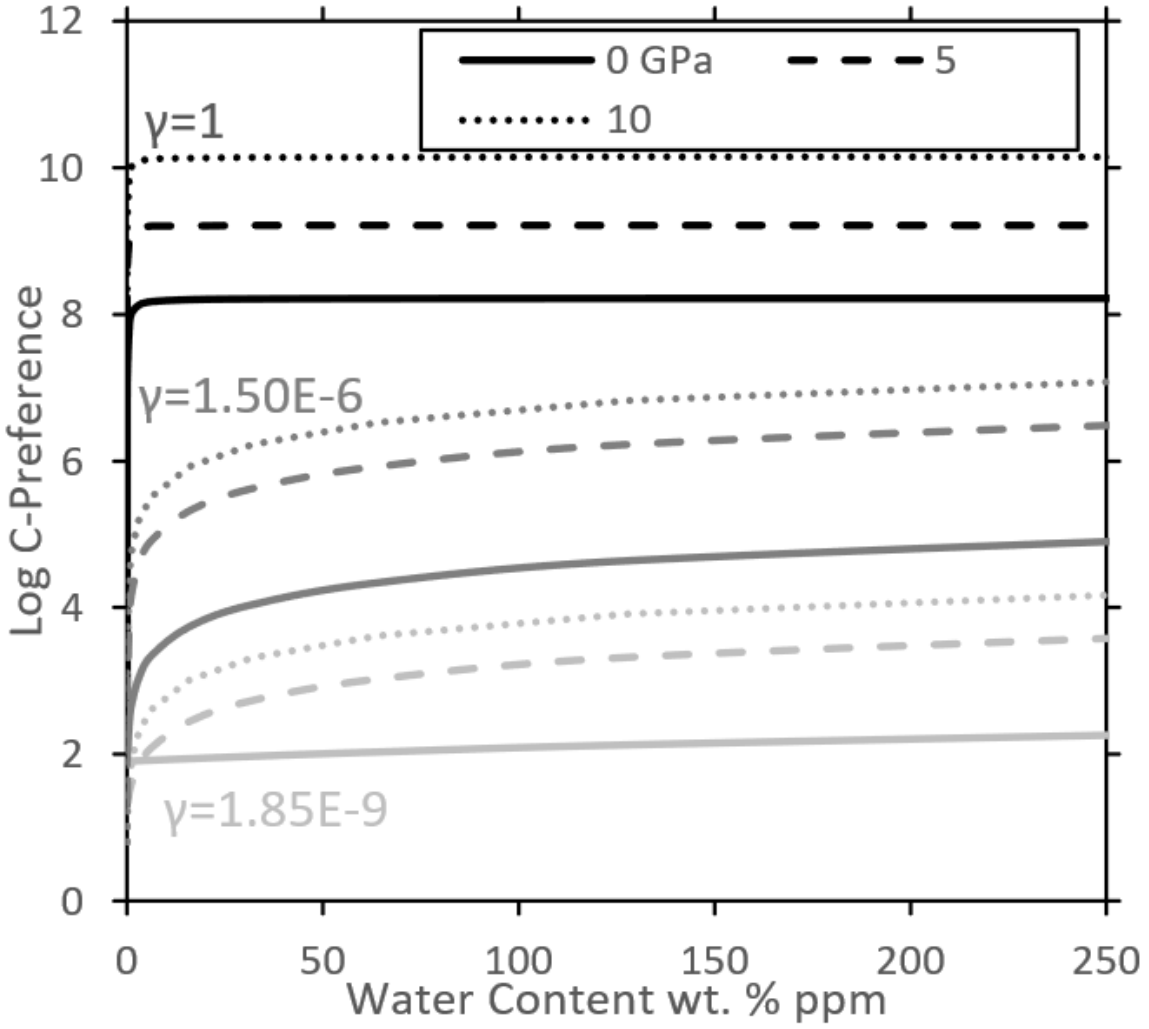

Figure 8: Plot of the C preference in forsterite as a function of water content at 1300 K (1000 and 1600 are plotted in Figure S7 and S8 but the effect of water and γ is very similar). C preference is defined as the $D_{[001]}/D_{[011]}$. Different pressures are shown with different line types (solid=0, dashed=5, dotted=10 GPa, all uncorrected). Different values for γ (Equation 1 and discussed more in text) are shown with different shades.

		0 Gpa	5	10
V''_{Mg}	M1	0	0	0
	M2	0.88	1.12	1.20
$(2H)^{X}_{Mg}$	M1	0	0	0
	M2	0.56	0.66	0.82
$Mg_{\ddot{I}nt}$	M1	-0.2	0.00	0.16
	I2	0	0	0

Table 1- Relative enthalpy of anhydrous and hydrous M1 and M2 vacancies and of anhydrous M1 and I2 interstitials.

	0 GPa	5	10
	Formation Energy (eV)		
0 K	5.65	6.43	6.54
1000	4.94	5.96	6.37
1300	4.73	5.78	6.27
1600	4.52	5.60	6.13
	Anhydrous Vacancy Concentration		
1000	4.13×10^{-13}	3.06×10^{-15}	9.23×10^{-17}
1300	8.51×10^{-10}	8.81×10^{-12}	9.37×10^{-13}
1600	9.59×10^{-08}	2.14×10^{-09}	2.89×10^{-10}
Water Vacancies (ppm wt%)			
	10	100	1000
	8×10^{-05}	8×10^{-04}	8×10^{-03}

Table 2: Free energy of the Frenkel reaction at various pressures and temperatures and the corresponding concentration of vacancies and interstitials (in defects/unit cell) in a perfect forsterite crystal where only the Mg frenkel reaction forms significant defects- this concentration is for each defect type so that the concentration of total defects (vacancies+interstitials) is twice this number. Also shown is the concentration of hydrated vacancies formed by water assuming water solely forms hydrated Mg vacancies (γ=1).

		Anhydrous Vacancy		Hydrated Vacancy		Anhydrous Interstitial	
		E_a (eV)	ν (Hz)	E_a (eV)	ν (Hz)	E_a (eV)	ν (Hz)
Hops from M1 Site							
A/G	M1-M1	0.75	1.01×10^{13}	1.26	2.90×10^{17}	3.22	9.11×10^{08}
B/H	M1-M1	4.12	3.71×10^{15}	3.81	2.82×10^{14}	3.16	1.22×10^{10}
C/I	M1-M2/I2	1.45	2.37×10^{14}	1.41	5.03×10^{13}	0.59	3.01×10^{09}
I*	M1-I2					1.35	2.38×10^{08}
D/J	M1-M2/I2	1.91	4.39×10^{14}	2.2	1.06×10^{14}	0.56	2.02×10^{09}
D*/J*	M1-M2/I2	1.91	4.39×10^{14}	2.2	1.06×10^{14}	1.29	2.80×10^{09}
Hops From M2/I2 Site							
C/I	M2/I2-M1	0.45	1.15×10^{14}	0.76	4.45×10^{12}	0.39	1.41×10^{13}
I*	M1-I2					1.15	1.11×10^{12}
D/J	M2/I2-M1	1.00	2.13×10^{14}	1.55	9.42×10^{12}	0.36	9.46×10^{12}
D*/J*	M2/I2-M1	1.00	2.13×10^{14}	1.55	9.42×10^{12}	1.09	1.31×10^{13}
E/K	M2/I2-M2/I2	1.65	4.27×10^{14}	1.87	1.86×10^{13}	1.08	5.53×10^{12}
F/L	M2/I2-M2/I2	2.82	2.31×10^{15}	2.8	7.21×10^{12}	N/A	N/A

Table 3: Activation energy and attempt frequency of various hops (shown in Figure 1 with the hop distances outlined in Table S1 and S2) for hydrous and anhydrous forsterite at 0 GPa. Hop L could not be stabilised but is very high in energy. Hops with an asterisk go in the reverse direction where it this is not equivalent.

		[100]	[010]	[001]
Anhydrous vacancy	1000 K	1.58×10^{-14}	6.61×10^{-14}	1.91×10^{-10}
	1300	3.37×10^{-12}	1.42×10^{-11}	1.48×10^{-09}
	1600	9.15×10^{-11}	4.02×10^{-10}	5.71×10^{-09}
Hydrous vacancy	1000	1.52×10^{-21}	4.37×10^{-17}	1.72×10^{-08}
	1300	5.90×10^{-19}	2.76×10^{-15}	4.58×10^{-07}
	1600	1.89×10^{-12}	8.73×10^{-12}	3.40×10^{-06}
Interstitial	1000	3.47×10^{-13}	7.58 X 10-13	2.65×10^{-13}
	1300	1.39×10^{-12}	3.62 X 10-12	1.18×10^{-12}
	1600	3.83×10^{-12}	7.86 X 10-12	3.96×10^{-12}

Table 4: Diffusion coefficients (m^2/s) of vacancies and interstitials in three directions at 0 GPa with 5 and 10 GPa coefficients listed in Table S7 and S8.

Supplementary Information for Highly Anisotropic Mg Diffusion in Forsterite: The Effect of Water by J M R Muir and A M Walker

Supplementary Methods

In this paper we calculate diffusion of Mg in forsterite through a 3 step process. In the first step we calculate the activation energy and frequency of various hops. In the second step we put these hopping results into a Kinetic-Monte Carlo algorithm (KMC). In the third step we combine the results of the KMC with a calculation of defect concentrations also calculated with DFT.

Each of these steps has additional information provided here. To validate our results in the first step and compare with previous work we also calculated the activation energies with forcefield calculations and the parameters of these calculations are outlined below. In the second step we use a KMC algorithm which is described briefly in the paper but is described fully below. In the third step we calculate defect concentrations by minimising the free energy. To do this we need to know the free energy of different concentrations of defects and the equations to calculate this are provided below.

Forcefield Calculations:

To compare our answers with earlier work we calculated hop energies using forcefield calculations. These calculations were done with GULP (Gale, 1997) and a forcefield designed for wet olivine (Wright and Catlow, 1994, Lewis and Catlow, 1985, Schroder et al., 1992). The parameters of this are given in Table S12**.** This potential reproduces the physical properties of forsterite reasonably well (Price et al., 1987) and has previously been used to model forsterite point defects as for example in Bejina et al. (2009) and Walker et al. (2009).

This potential models cations with a formal charge (Mg 2+, Si 4+) whereas O atoms are modelled as a positively charged core (+0.84819) with a negatively charged massless shell (-2.84819). All cation-anion pairs are joined by a Buckingham potential and SiO_4 tetrahedra are fixed with a harmonic three body potential. H^+ ions in this potential are represented by O-H groups using a Morse potential where the participating oxygen ion is represented by a partially ionic point charge. To place the hydrogen we used the most stable arrangements of hydrogen that were determined by DFT- in M1 vacancies both H are bound to an O2 atom, in M2 vacancies one is bound to an O1 and one to an O3 atom.

Columbic energy was calculated using the Wolf sum (Wolf et al., 1999) which uses a charge neutralizing term to guarantee convergence of the energy at a finite distance. Its cutoff was set to 15 Å with a damping parameter x=0.2 $Å^{-1}$. For charged systems a neutralising uniform charged background was added.
We used the same unit cells (2x2x1) as for DFT cells and also a cell that was twice as large (4x4x2). Doubling the cell size changed the activation of the hops by <100 meV.

Two methods were used to find the transition state of the hops. Firstly we used the constrained optimisation method that is outlined in the methods for DFT calculations. Then we took the resulting optimisation state and used the RFO optimisation routine in GULP to find the nearest stationery point with 1 negative frequency. This second step changed our activations by less than 10 meV which shows that our constrained optimisation method produces transition states that are reasonably accurate.

Kinetic Monte Carlo Algorithm

In this section we shall describe our KMC algorithm while a flow diagram presenting the same information is shown in Figure S8. For each state (e.g. a vacancy on M1 or a vacancy on M2) we evaluate the rate of each of the k^i hops escaping from that state (equation 8 using equations 9), sum these to give k^{tot} and calculate the probability of each hop from $p^i = \frac{k^i}{k^{tot}}$. This provides a "transition matrix", which encodes the probability of each transition from a given starting state to each reachable final state. Symmetrically equivalent hops in different directions are included separately in this matrix. We separately store the jump vectors for each transition in the matrix, "unwrapping" the periodicity of the crystal. Our algorithm is initialised by choosing an initial state, a start time, and position for the defect. We then proceed as follows:

1) Draw two uniform random numbers (r^1 and r^2) from the interval [0,1].
2) Using r^1 select a hop out of the current state based on weighted probabilities p^i by placing the probabilities of each hop (p^i) end to end in a line from 0 to 1 and then selecting the hop that occurs at r^1 along the line (see Fig S2 and Fig S3).
3) Using r^2 determine the time spent in the state:

$$t^i = -\left(\frac{1}{k_{tot}}\right)\ln(r^2)$$ Equation S1

4) Update the state index and defect position using the selected hop, advance time by t^i
5) Return to 1

As this algorithm progresses, we build a list of positions of the defect as a function of time as it undergoes a random walk through the (infinite) crystal structure. This is the information we need to calculate the diffusion coefficient from the mean squared displacement (MSD).

Calculating the MSD with non-equidistant time steps is not straightforward and doing this with error propagation particularly cumbersome. A rigorous method of MSD and error calculation for non-equidistant timesteps has been presented by Leetmaa and Skorodumova (2015) and has been used in this work. After every hop (step 4) we compare the current position of the particle and the time with the particle positions and the time for the previous N simulation steps where N is referred to as the history window. For each comparison the squared displacement is calculated and these are then binned by the difference in time into a histogram D(t) with the number of squared displacements in each bin recorded as a separate histogram H(t). Mean squared displacement for each bin (ρ_i) is then:

$\rho_i = D_i/H_i$ Equation S2

which is then plotted against time (see for example Figure S9) with the time of each bin taken as the centre of that bins time window. The MSD $\langle x^2 \rangle$ trace is related to diffusion by:

$\langle x^2 \rangle = q_i D t$ Equation S3

so that the diffusion coefficient D can be found by calculating the slope of $\langle x^2 \rangle$ against $q_i t$. In all of our calculations the total number of runs (M) was 50,000,000, the history window (N) was 50,000, 200,000 bins were used to bin across a time that varied depending upon the simulation. In this formulation N controls the total length of diffusion whereas M controls the accuracy/number of samplings. Standard deviation of our data was calculated using the method in Leetmaa and Skorodumova (2015) using the infinite limit for ne(t) as our N values are large.

As a test of this method we calculated the diffusion rate of Mg diffusion in MgO. This was determined analytically in Vocadlo *et al.* (1995) and our KMC method produced diffusion rates that were within 1% of the analytical values ($1.76*10^{-27}$ vs $1.78*10^{-27}$ m/s^2) even with quite low MSD parameter cutoffs (M=2,000,000, N=20,000)

<u>Finding the equilibrium concentration of defects:</u>

To calculate diffusion we need to know the concentration of defects in our system.

We assume the Mg Frenkel reaction (Reaction 1) is the primary source of intrinsic Mg defects in forsterite:

$Mg_{Mg}^{X} \rightarrow V_{Mg}'' + Mg_I^{\bullet\bullet}$ Reaction 1

We can calculate the equilibrium concentration of defects by calculating the free energy minimum of this reaction.

This is not entirely straightforward due to the fact that Mg interstitials can easily two different sites (M1 and I2) with little energy difference between them (Table 1). We thus need to use a Gibb's entropy calculation to work out the probability of Mg interstitials occupying the different sites and the configuration entropy that results.

This is done as follow. We first calculate the reaction energy (ΔE) of R1 which is the enthalpy and vibrational energy change of proceeding Reaction 1 to the right. We define a reaction vector (a) which is between 0 and 1 and which determines how far R1 proceeds to the right with 0 being the production of no defects and 1 being the production of entirely defects. This x also defines the concentration of vacancies and interstitials that are produced.

Free energy as a function of a is then determined using the following equation:

$\Delta G = \Delta E \times a - TS_{confa}$ Equation S4

Where S_{confa} is the configurational entropy at a. This configurational entropy term is determined in the following way. We have 2 defects (vacancy and interstitial) which can each occupy two sites M1 and M2 for vacancies, M1 and I2 for interstitials. We thus define 4 configurations (i) where the defects of each type are confined to a respective vacancy {Vacancy on M1/Interstitial on M1, M1/I2, M2/M1, M2/I2}. The internal energy of each configuration (U_i) was then calculated using Table 1 with the assumption that temperature does not affect the relative energy of placing defects on different sites. We must then calculate the degeneracy of each configuration (W) which is done using:

$W=\ln\frac{N!}{a!b!\ldots z!}$ Equation S5

Where N is the total number of sites, and a,b,c…z are the different types of atoms/defects at each site including a final z term, which is simply (N-a-b….-y). To solve this numerically, all defect concentrations were written in terms of defects/mol and then the Stirling approximation was used ($lnn! \cong nln - n$), giving:

$W = NlnN - N - alna + a - blnb + b \ldots - zlnz + z$ Equation X

To calculate the configurational entropy we then need to know the probability and entropy of each of these configurations. We calculate this using the Gibbs entropy formula:

$S_{confa} = -k_B \sum_j p_j lnp_j$ Equation S6

Where k_B is the Boltzmann constant. j in Equation S6 represents a specific configuration (i) but in j each configuration (i) appears an equal number of times to its degeneracy (w). p_j represents the probability that each j configuration occurs. The probability of any specific configuration occurring is:

$$p_j = \frac{1}{Z} e^{(-U_j/k_B T)}$$ Equation S7

Where Z is the canonical partition function

$$Z = \sum_j e^{(-U_j/k_B T)}$$ Equation S8

Equation S6 can then be calculated and this energy added into Equation S4. The reaction vector a in Equation S4 can then be varied until a free energy minimum is found. This then tells us how far forward R1 proceeds at equilibrium and thus the concentration of defects at equilibrium.

Supplementary Results

In our work we simulate diffusion through a series of atomistic hops. These hops are pictured in the text but both vacancy and interstitial hops shall be described below. In our work we also found that water has an effect on activation energy of various vacancy hops. This does not have a large effect on our results as this change is much smaller than concentration and attempt frequency changes in a hydrous system but we shall discuss possible reasons for it below.

Vacancy Hops:

The vacancy hops that we study in this work are an A hop (F in Walker *et al.* 2009) between two M1 sites along the [001] direction, a B (A) hop between two M1 sites along the [100] direction through an I1 site, a C (D) and D (E) hop between M1 and M2 sites along the [011] and [111] directions respectively, an E (C) hop between two M2 sites along the [101] direction and an F (B) hop between two M2 sites along the [100] direction through an I2 site. Of the hops that we ruled out there are two important ones. First a direct [001] hop between two M2 sites (analogous to the A hop on the M1 sites) was found to have an activation energy of 4.65 eV, much higher than two E hops which will achieve the same outcome. Second a direct [101] hop between two M1 sites- analogous to the E hop on the M2 sites was found to have a very high activation energy of >7.8 eV due to the presence of both Si and M2 atoms along any possible route.

Interstitial Hops:

The interstitial hops that are studied are a G hop between two M1 sites along [001], a H hop between two M1 sites along [100] through an I1 site, hops I and J between the M1 and I2 sites along [011] and [111], respectively, a K hop between two I2 sites along [101] and a L hop between two I2 sites along [100] through an M2 site.

The effect of water on activation energies of hops:

Water has a varied effect on the activation energy of vacancy hops with $\Delta_{Hydration}$ (E_{actwet}-E_{actdry}) occurring as both positive and negative terms when considering different hops. This is a small effect when compared to the effect water has on attempt frequency but is still curious.

There is a weak trend of $\Delta_{Hydration}$ (E_{actwet}-E_{actdry}) decreasing with length of the hop. Water has two effects on the migration of Mg vacancies. The first effect is that the H^+ atoms balance out the charge of the vacancy which makes it easier to move a charged Mg^{2+} atom out of its initial position and reduces the activation energy. A converse effect is that placing 2 H^+ atoms in the vacancy causes interatomic repulsion which makes it harder to move a charged Mg^{2+} atom and increases the activation energy. At shorter ranges the latter effect will dominate and activation energies will increase while at longer ranges the former effect becomes important and activation energies decrease. These two trends can be demonstrated with force field calculations (Figure S10) creating a $\Delta_{Hydration}$ trend with distance (Figure S11) in the forcefield results. This trend is less clear in DFT calculations which more accurately consider these effects but the somewhat unusual effect on water on activation energies remains

Supplementary Information Bibliography

BEJINA, F., BLANCHARD, M., WRIGHT, K. & PRICE, G. D. 2009. A computer simulation study of the effect of pressure on Mg diffusion in forsterite. *Physics of the Earth and Planetary Interiors,* 172**,** 13-19.

GALE, J. D. 1997. GULP - a computer program for the symmetry adapted simulation of solids. *JCS Faraday Trans,* 93**,** 629-637.

LEETMAA, M. & SKORODUMOVA, N. V. 2015. Mean square displacements with error estimates from non-equidistant time-step kinetic Monte Carlo simulations. *Computer Physics Communications,* 191**,** 119-124.

LEWIS, G. V. & CATLOW, C. R. A. 1985. POTENTIAL MODELS FOR IONIC OXIDES. *Journal of Physics C-Solid State Physics,* 18**,** 1149-1161.

PRICE, G. D., PARKER, S. C. & LESLIE, M. 1987. THE LATTICE-DYNAMICS OF FORSTERITE. *Mineralogical Magazine,* 51**,** 157-170.

SCHRODER, K. P., SAUER, J., LESLIE, M., CATLOW, C. R. A. & THOMAS, J. M. 1992. BRIDGING HYDROXYL-GROUPS IN ZEOLITIC CATALYSTS - A COMPUTER-SIMULATION OF THEIR STRUCTURE, VIBRATIONAL PROPERTIES AND ACIDITY IN PROTONATED FAUJASITES (H-Y ZEOLITES). *Chemical Physics Letters,* 188**,** 320-325.

WALKER, A. M., WOODLEY, S. M., SLATER, B. & WRIGHT, K. 2009. A computational study of magnesium point defects and diffusion in forsterite. *Physics of the Earth and Planetary Interiors,* 172**,** 20-27.

WOLF, D., KEBLINSKI, P., PHILLPOT, S. R. & EGGEBRECHT, J. 1999. Exact method for the simulation of Coulombic systems by spherically truncated, pairwise r(-1) summation. *Journal of Chemical Physics,* 110**,** 8254-8282.

WRIGHT, K. & CATLOW, C. R. A. 1994. A computer simulation study of (OH) defects in olivine. *Physics and Chemistry of Minerals,* 20**,** 515-518.

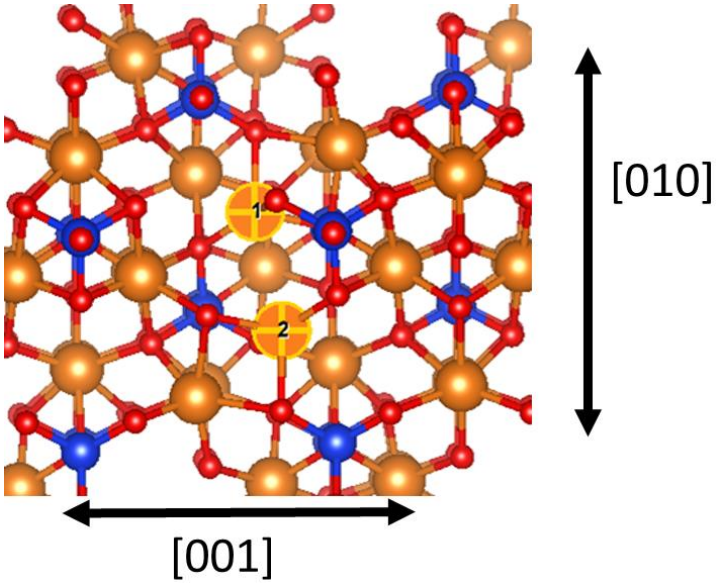

Figure S1: Diagram of the split interstitial Mg arrangement with the two Mg that split across the M1 site highlighted.

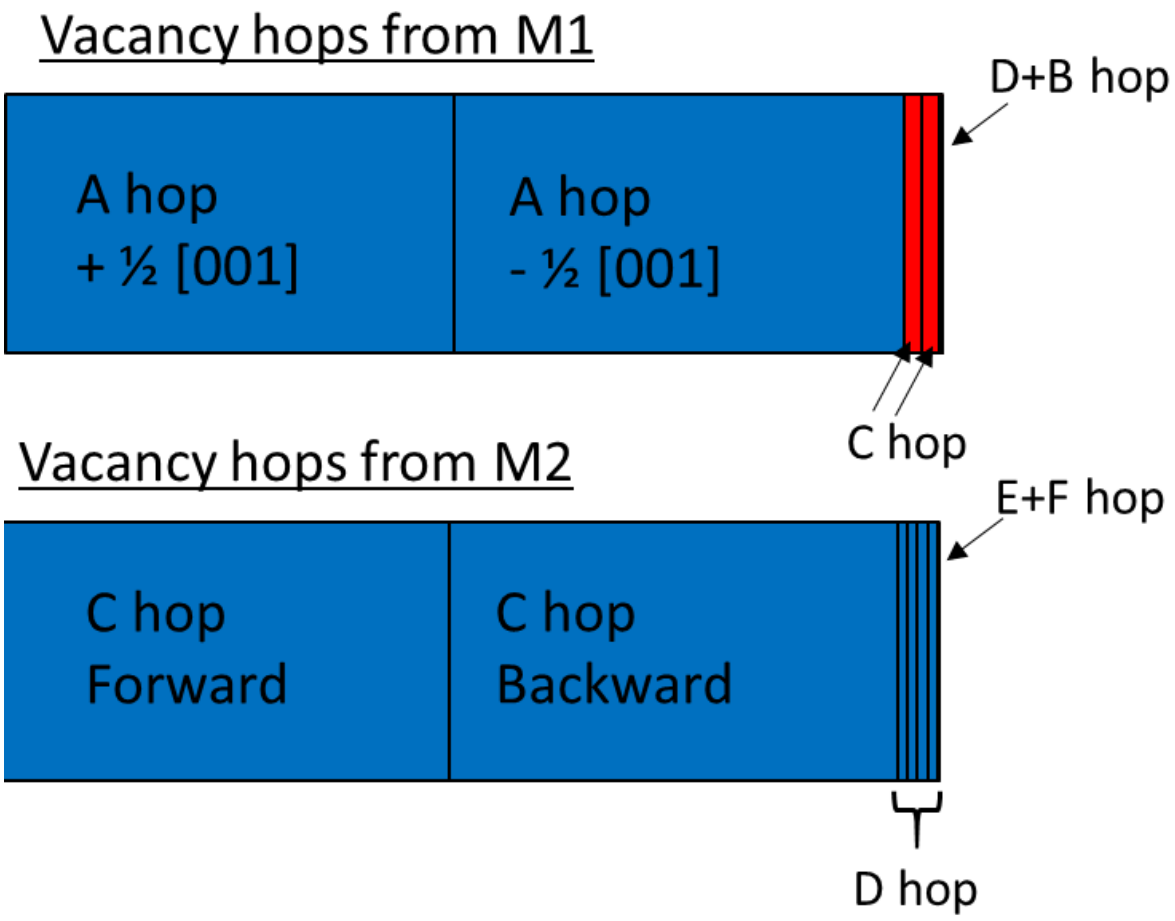

Figure S2: Plot of the different vacancy hops from an M1 and M2 site weighted by the probability of undergoing that hop (determined at 0 GPa and 1300 K). Hops coloured in blue end up in an M1 site, hops coloured in red end up in an M2 site.

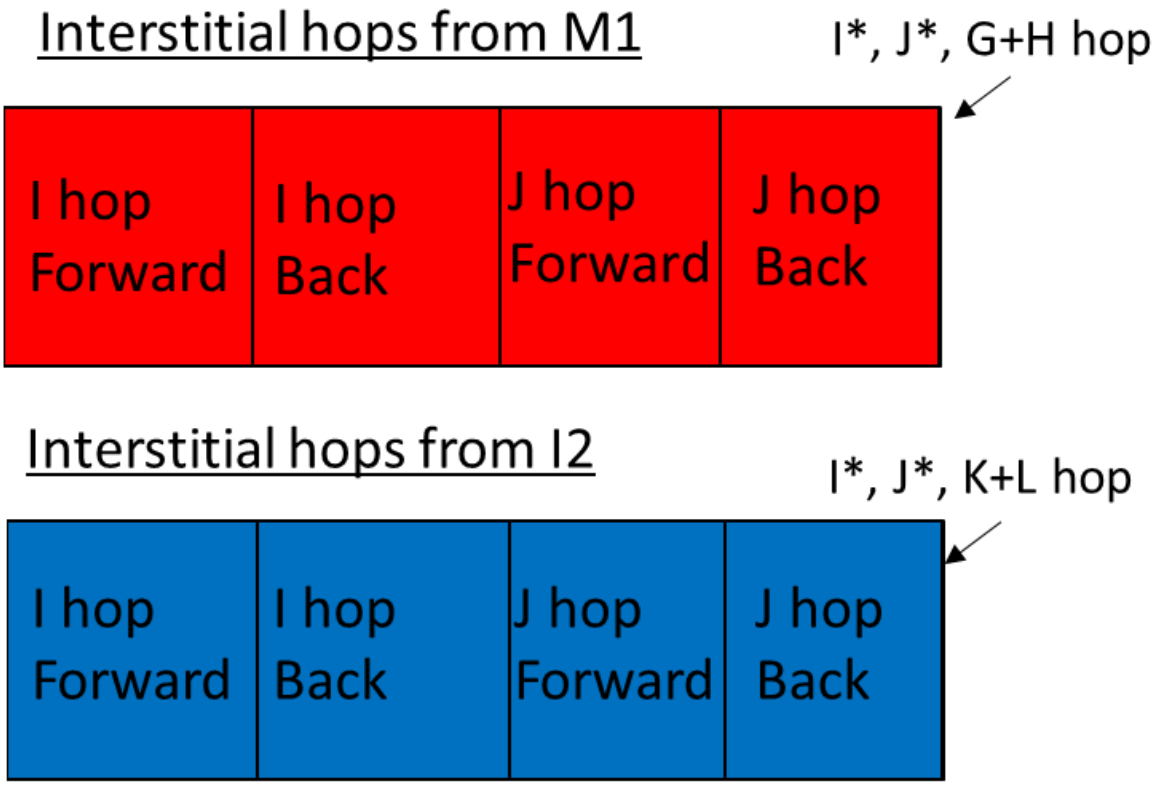

Fig S3: As Figure S2 but for interstitial hops. Hops coloured blue end up on an M1 site, red an I2 site.

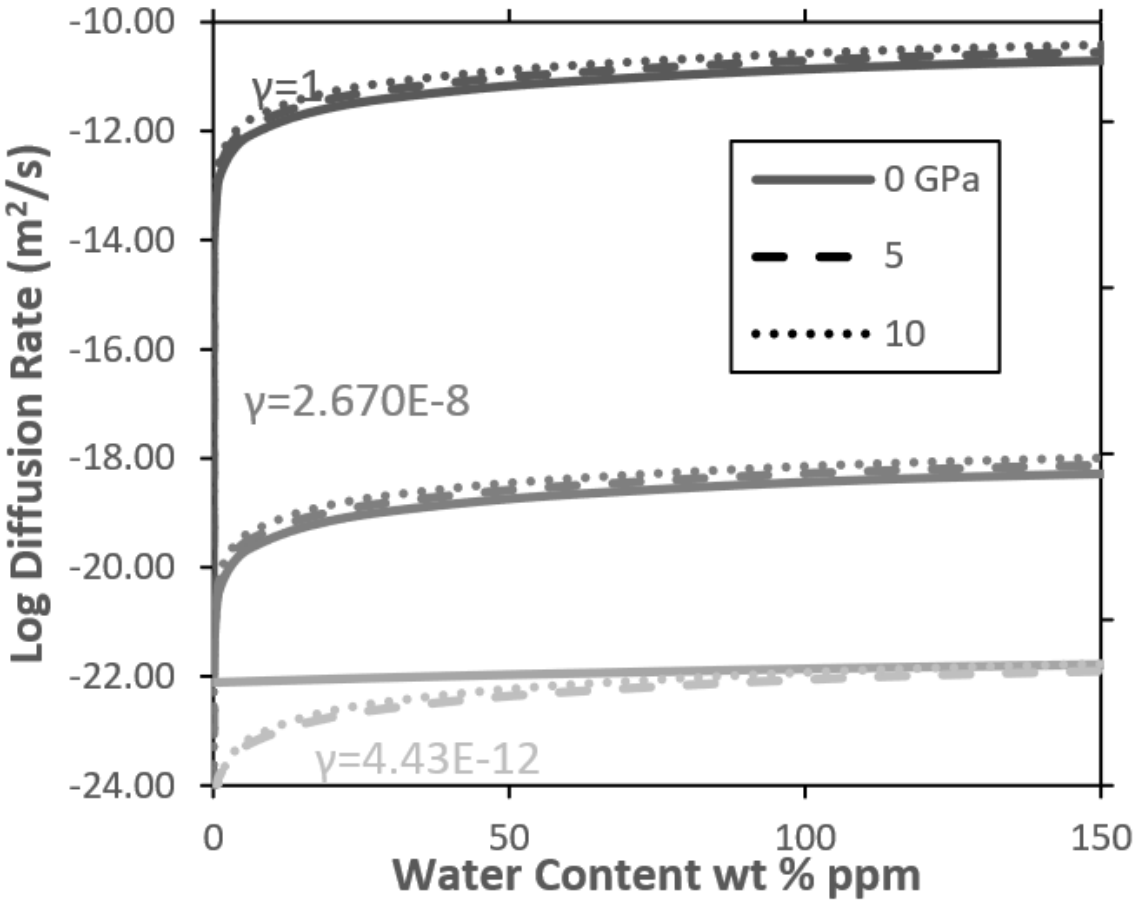

Fig S4 As Figure 7 but for 1000 K.

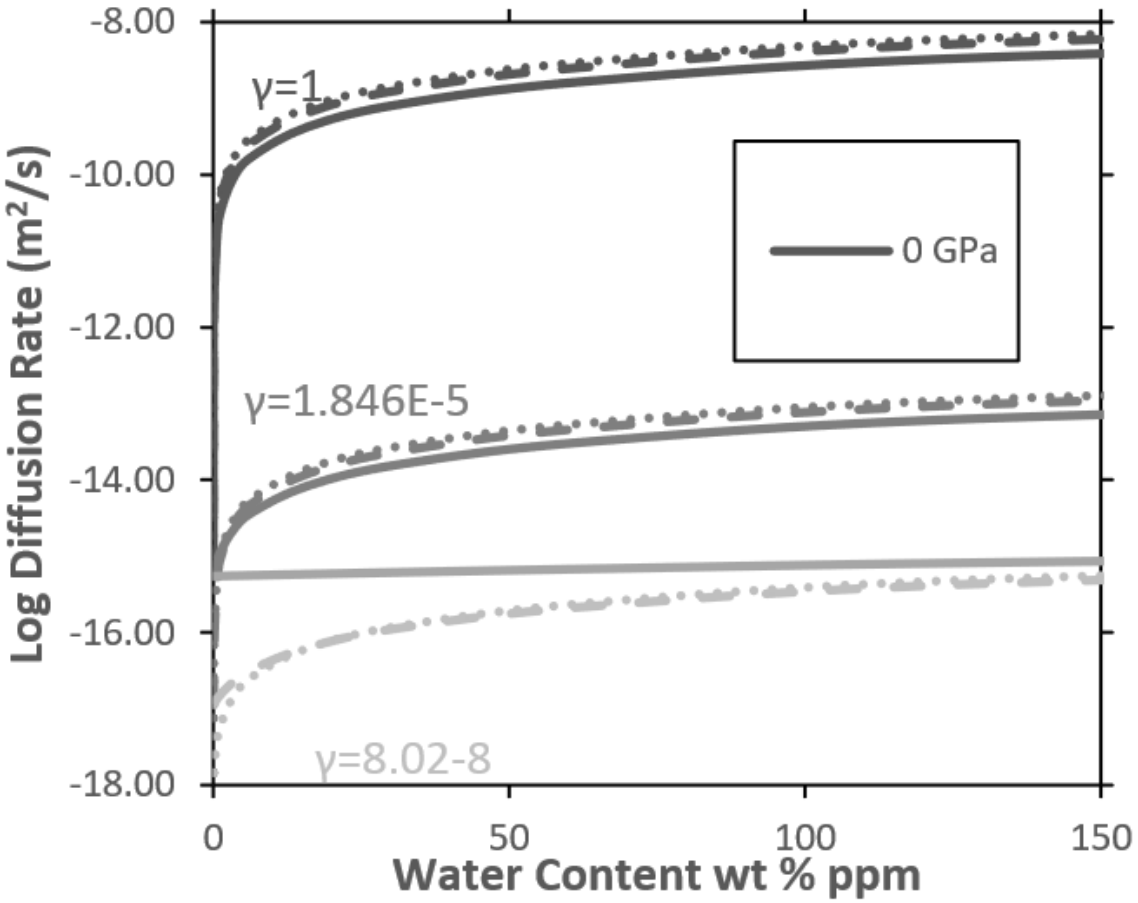

Fig S5 As Figure 7 but for 1600 K.

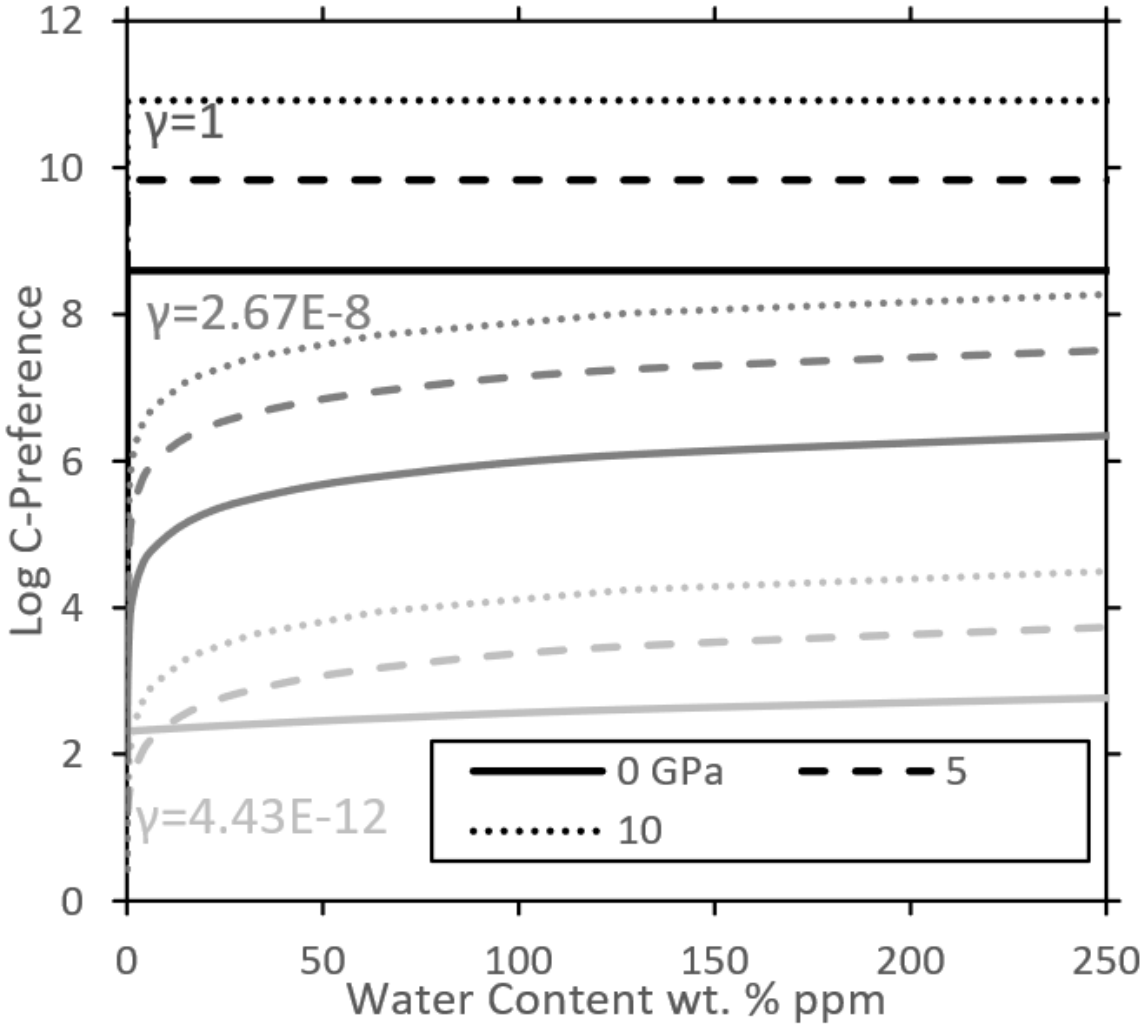

Fig S6 As Figure 8 but for 1000 K

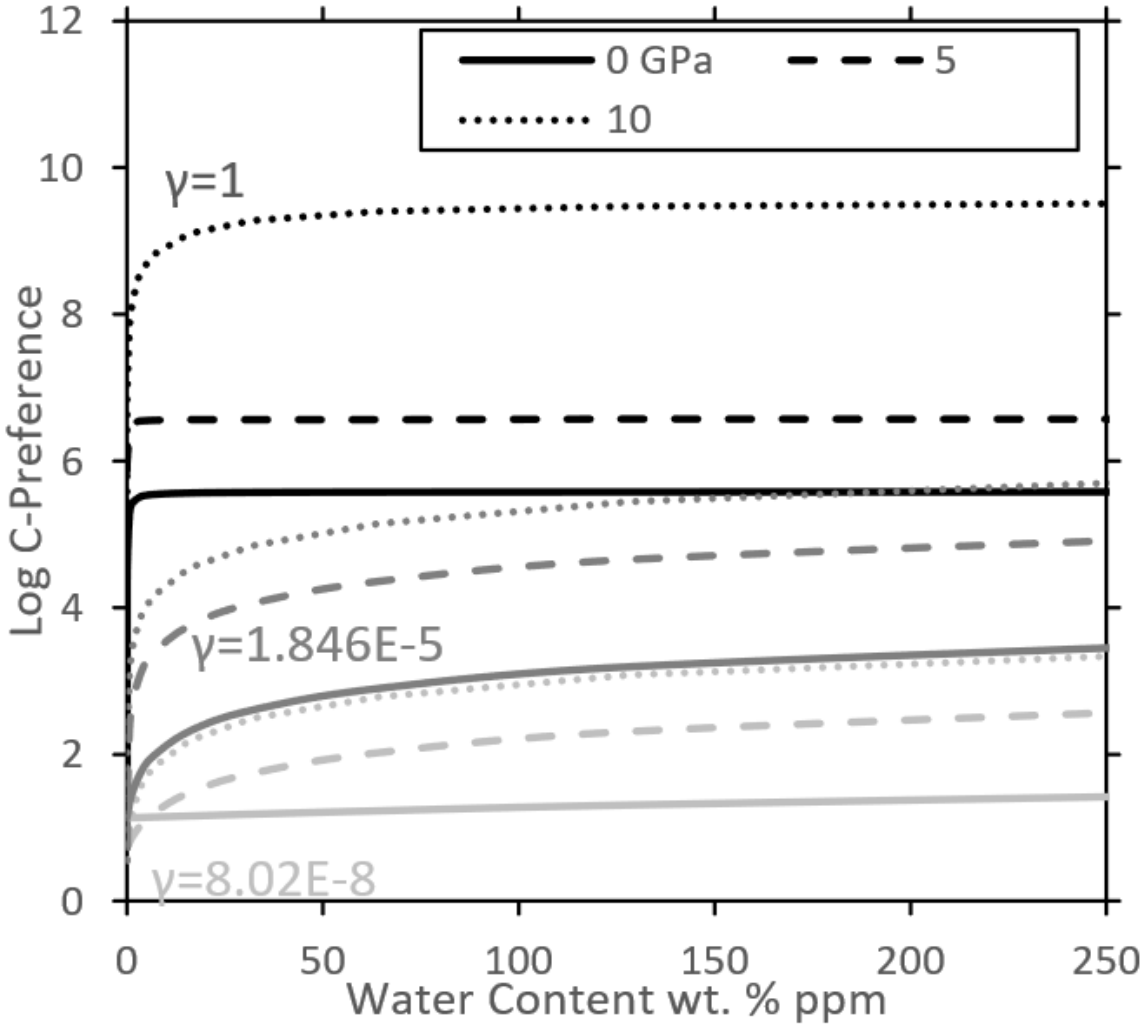

Fig S7 As Figure 8 but for 1600 K

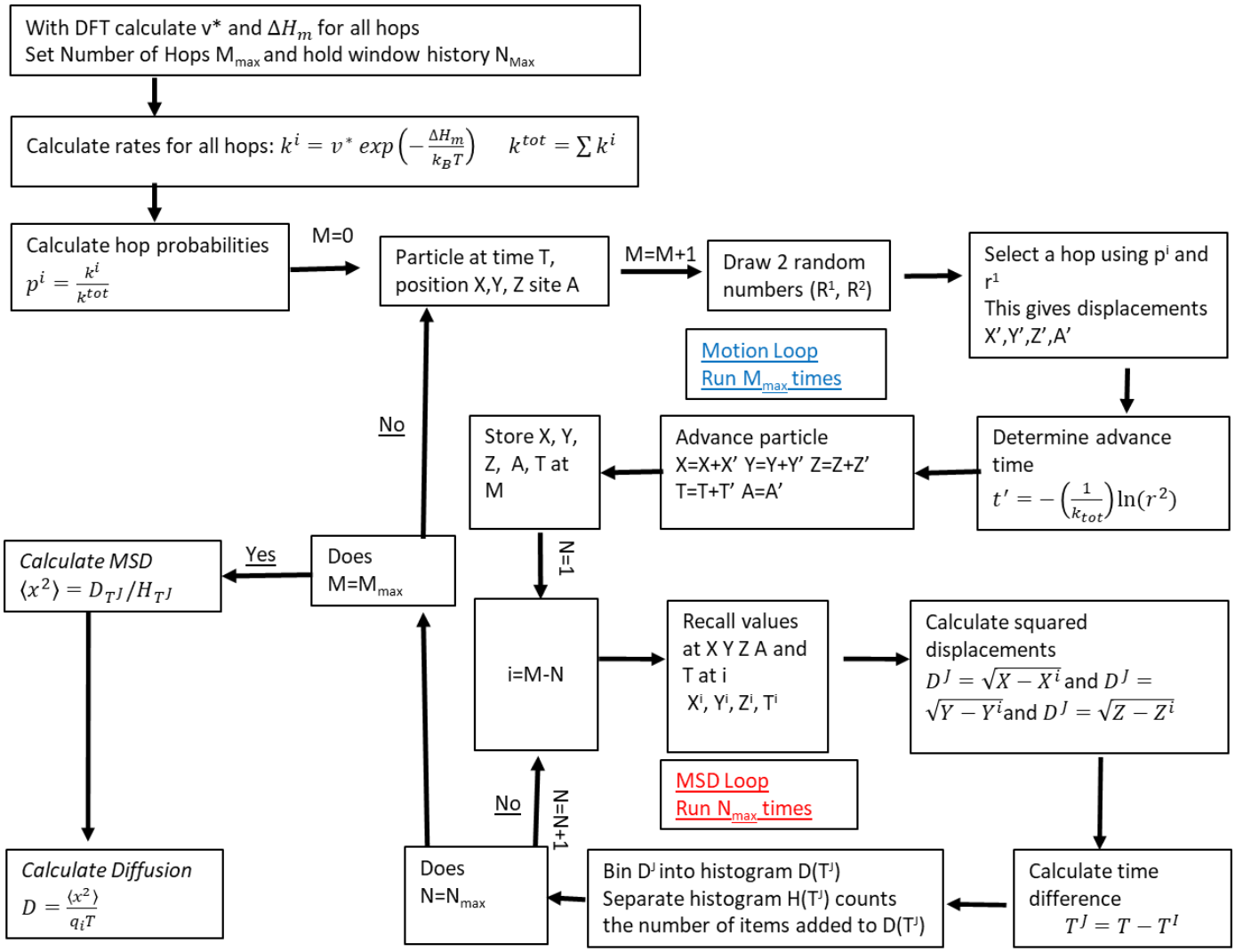

Figure S8: Flow diagram showing the main logic of the MSD and KMC algorithm. There are two loops- the second MSD loop can be run either at the end after all motion steps have been calculated or simultaneously with the motion steps as shown here.

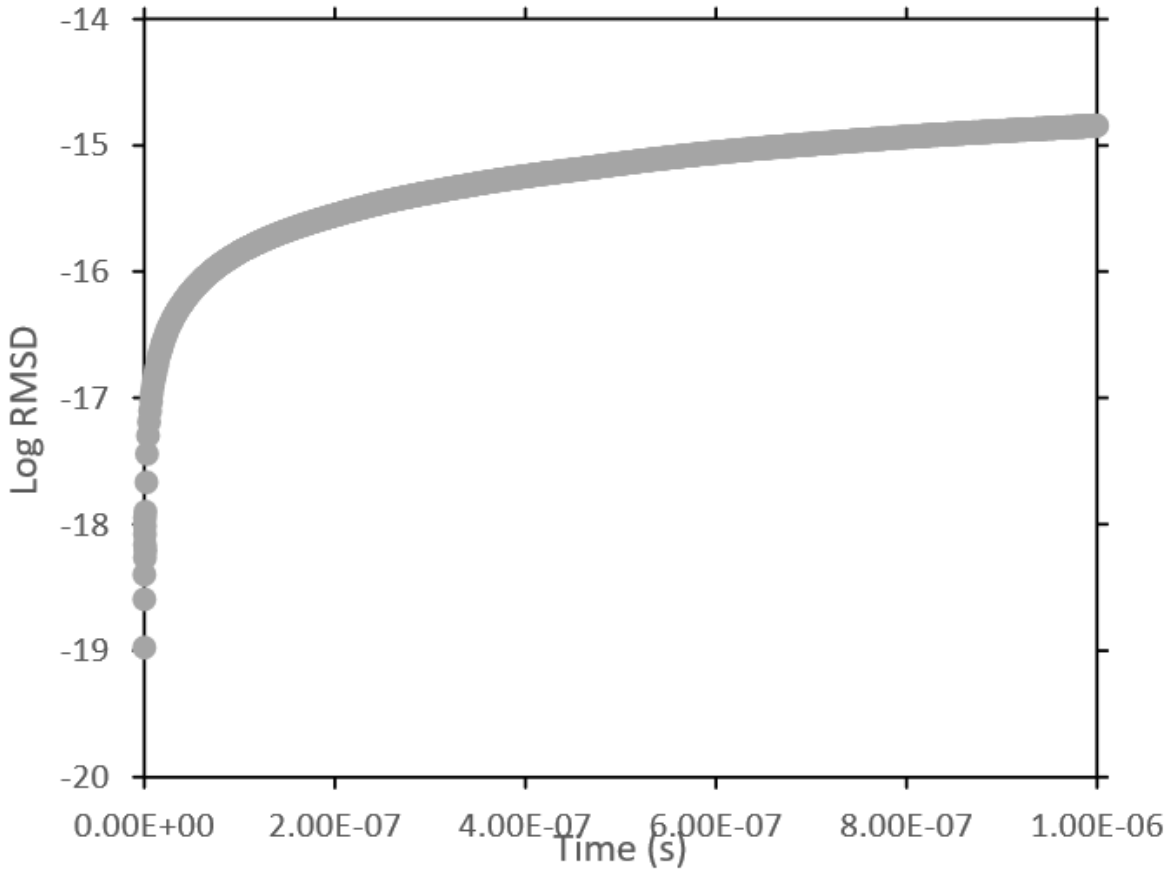

Figure S9: Sample graph showing the log of the RMSD against time for an [001] vacancy hop at 1300 K. Diffusion can be calculated by calculated the slope of the RMSD vs T. Diffusion is determined by the trend of the RMSD vs time but the earliest time steps (before a linear trend is reached) are discarded as diffusion is defined against the long-time limit.

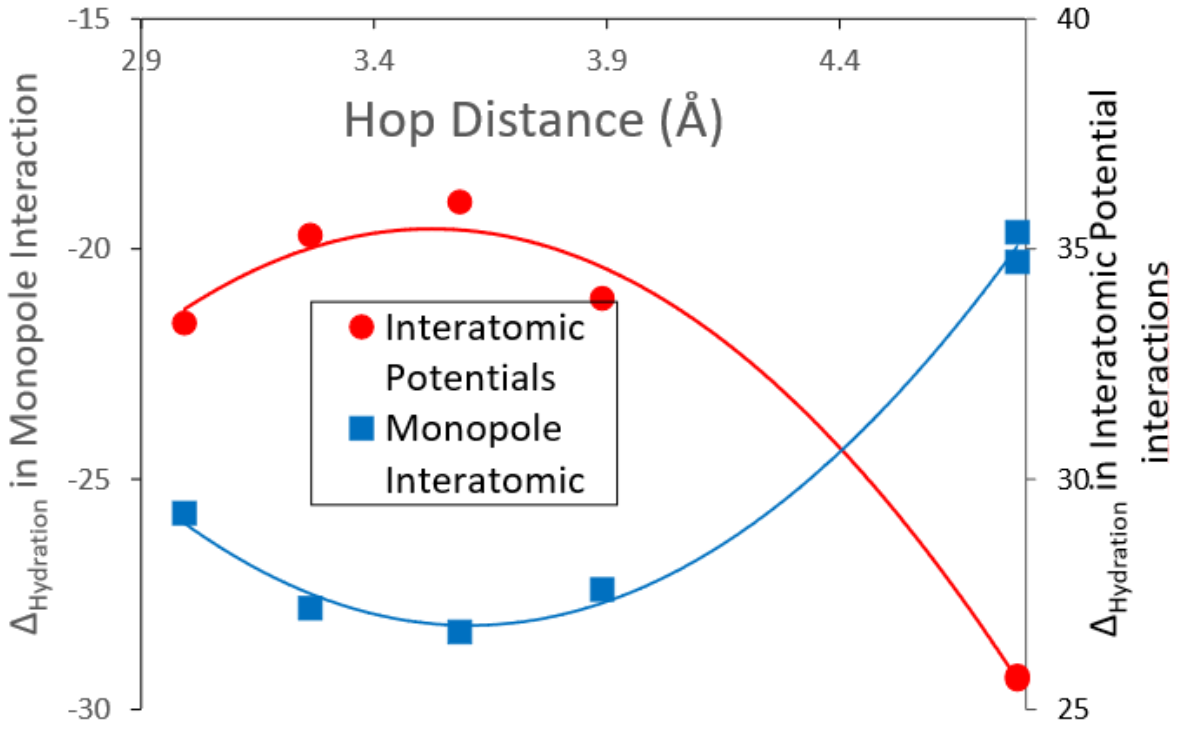

Figure S10: Variation in monopole-monopole interactions and interatomic potential interactions between wet and dry vacancy hops (wet-dry) as a function of hop distance for forcefield calculations at 0 GPa.

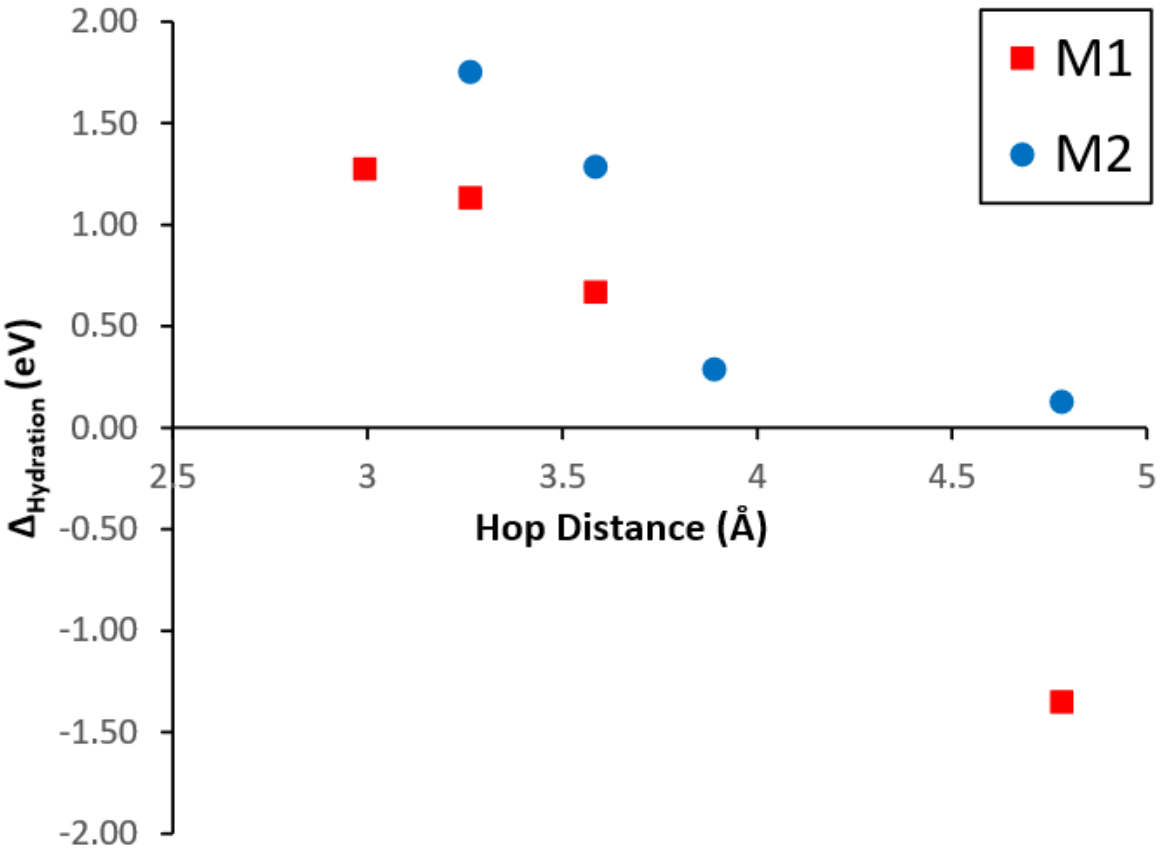

Figure S11: $\Delta_{Hydration}$ for forcefield calculations as a function of vacancy hop distance. Points are colour coded by whether they are hops from an M1 or an M2 site. There is a weak trend of $\Delta_{Hydration}$ decreasing with distance as explained in the text. More accurate DFT results have an even weaker trend but still generally decrease $\Delta_{Hydration}$ with distance.

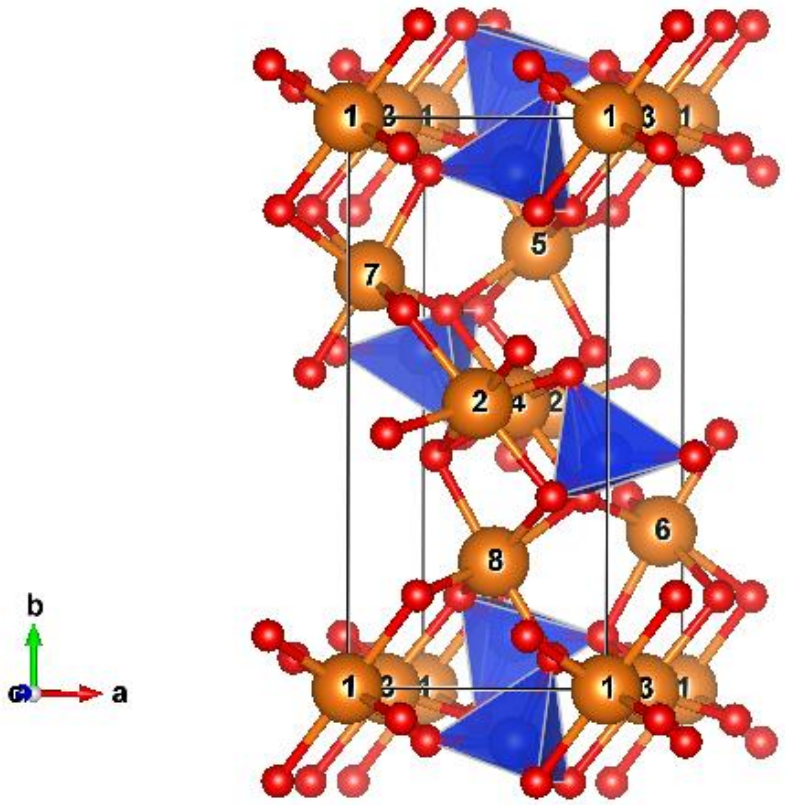

Figure S12: Unit cell of forsterite with labelled magnesium for reference in Table S1 and S2.

Site	[100]	[010]	[001]	Degeneracy	Hops between sites starting from 1/5	Possible Directions from Sites 1/5
Vacancy Hops from M1						
A	0.000	0.000	0.500	2	1-3	+c,-c
B	1.000	0.000	0.000	2	1-1	+a,-a
C	0.009	0.277	0.250	2	1-6/7	-a +b +c, +a -b -c
D	0.491	0.223	0.250	2	1-5/8	-a -b +c, +a +b -c
D*	0.509	0.223	0.250	2	1-5/8	+a -b +c, -a +b -c
Vacancy Hops From M2 Site						
C	0.009	0.277	0.250	2	5-2/4	-a -b -c, -a -b +c
D	0.491	0.223	0.250	2	5-1/3	+a +b -c, +a +b +c
D*	0.509	0.223	0.250	2	5-1/3	-a +b -c, -a +b +c
E	0.500	0.055	0.500	4	5-7	+a -b +c, +a -b -c, -a -b +c, -a -b -c
F	1.000	0.000	0.000	2	5-5	+a,-a

Table S1: List of different vacancy hops and their absolute hop distance in unit cell values (at 0 GPa these are 4.80, 10.32 and 6.04 Å respectively) and their degeneracy. To illustrate the degeneracy of the hops we have shown the possible hops between different sites and the different degenerate directions with hops starting from site 1 (an M1 site) and from site 5 (an M2 sites) (with atom labels in Figure S12).

Site	[100]	[010]	[001]	Degeneracy	Hops between sites starting from 1/13	Possible Directions from Sites 1/13
Interstitial sites from M1						
G	0.000	0.000	0.500	2	1-3	+c,-c
H	1.000	0.000	0.000	2	1-1	+a,-a
I	0.009	0.277	0.250	2	1-13/16	-a +b -c, +a -b +c
I*	0.009	0.277	0.250	2	1-14/15	-a -b -c, +a +b +c
J	0.491	0.223	0.250	2	1-14/15	+a -b -c, -a +b +c
J*	0.509	0.223	0.250	2	1-3	+c,-c
Interstitial Hops from I2						
I	0.009	0.277	0.250	2	13-1/3	-a +b -c, -a +b +c
I*	0.009	0.277	0.250	2	13-2/4	+a -b +c, +a -b -c
J	0.491	0.223	0.250	2	13-2/4	-a -b +c, -a -b -c
J*	0.509	0.223	0.250	2	13-15	+a -b +c, +a -b -c, -a -b +c, -a -b -c
K	0.500	0.055	0.500	4	13-13	+a,-a
L	1.000	0.000	0.000	2	13-1/3	-a +b -c, -a +b +c

Table S2: List of different interstitial hops and their absolute hop distance in unit cell values (at 0 GPa these are 4.800, 10.32 and 6.04 Å respectively) and their degeneracy. As I2 sites are simply M2 sites shifted by 0.5 in the A direction these hops are the same as the vacancy hops but M1-I2 hops go in different relative directions than M1-M2 hops.

		Anhydrous			Hydrous		$\Delta_{Hydration}$	
	Distance	Walker	Gulp	CASTEP	Gulp	CASTEP	Gulp	CASTEP
A	2.99	0.72	0.77	0.75	2.04	1.26	1.27	0.51
C-M1	3.26	1.96	2.10	1.45	3.23	1.41	1.13	-0.04
C-M2	3.26	0.06	0.19	0.45	1.95	0.76	1.75	0.31
D-M1	3.58	4.54	2.28	1.99	2.95	2.20	0.67	0.21
D-M2	3.58	6.64	0.37	1.00	1.65	1.55	1.28	0.56
E	3.89	1.47	2.53	1.63	2.82	1.87	0.29	0.24
B	4.78	5.89	6.06	4.12	4.71	3.81	-1.35	-0.31
F	4.78	9.1	3.96	2.82	4.09	2.80	0.13	-0.02

Table S3: Comparison of anhydrous and hydrous activation energies from forcefield calculations in literature (Walker *et al.* 2010) and with our DFT CASTEP calculations and additional calculations done with the TBH1 forcefield. Additionally we show the distance of the hop (at 0 GPa with CASTEP calculations) and the difference in activation energy between anhydrous and hydrous hops. Hop distances are in Å and activation energies in eV.

		Anhydrous			Hydrous		
		0 GPa	5	10	0 GPa	5	10
Hops From M1 Site							
A	M1-M1	0.75	0.75	0.75	1.26	1.23	1.20
B	M1-M1	4.12	4.29	4.63	3.81	4.21	4.53
C	M1-M2/	1.45	1.52	1.63	1.41	1.64	1.82
D	M1-M2/	1.99	1.92	1.85	2.20	2.47	2.68
D*	M1-M2/	1.99	1.92	1.85	2.20	2.47	2.68
Hops From M2 Site							
C	M2-M1	0.45	0.45	0.47	0.76	0.85	0.96
D	M2-M1	1.00	0.84	0.69	1.55	1.68	1.82
D*	M2-M1	1.00	0.84	0.69	1.55	1.68	1.82
E	M2-M2	1.63	1.72	2.00	1.85	2.08	2.31
F	M2-M2	2.87	2.97	3.30	2.80	3.18	3.46

Table S4: Variation in activation energy (in eV) of vacancy hops with pressure

		Anhydrous Vacancy			Hydrous Vacancy			Anhydrous Interstitial		
		0 GPa	5	10	0 GPa	5	10	0 GPa	5	10
Hops from M1 Site	A/G	1.01×10^{13}	1.08×10^{13}	1.23×10^{13}	2.90×10^{17}	3.09×10^{17}	3.53×10^{17}	9.11×10^{8}	9.70×10^{8}	1.11×10^{9}
	B/H	3.71×10^{15}	2.95×10^{15}	2.36×10^{15}	2.82×10^{14}	2.21×10^{14}	1.79×10^{14}	1.22×10^{10}	9.52×10^{9}	7.71×10^{9}
	C/I	2.37×10^{14}	2.43×10^{14}	2.57×10^{14}	5.03×10^{13}	5.16×10^{13}	5.46×10^{13}	3.01×10^{9}	3.08×10^{9}	3.26×10^{9}
	I*							2.38×10^{8}	2.44×10^{8}	2.64×10^{8}
	D/J	4.39×10^{14}	4.43×10^{14}	4.59×10^{14}	1.06×10^{14}	1.07×10^{14}	1.11×10^{14}	2.02×10^{9}	2.04×10^{9}	2.14×10^{9}
	D*/J*	4.39×10^{14}	4.43×10^{14}	4.59×10^{14}	1.06×10^{14}	1.07×10^{14}	1.11×10^{14}	2.80×10^{9}	2.83×10^{9}	2.96×10^{9}
Hops From M2/I2 Site	C/I	1.15×10^{14}	1.51×10^{14}	2.07×10^{14}	4.45×10^{12}	5.84×10^{12}	8.00×10^{12}	1.41×10^{13}	1.85×10^{13}	2.53×10^{13}
	I*							1.11×10^{12}	1.46×10^{12}	2.00×10^{12}
	D/J	2.13×10^{14}	2.70×10^{14}	3.36×10^{14}	9.40×10^{12}	1.19×10^{13}	1.48×10^{13}	9.46×10^{12}	1.20×10^{13}	1.49×10^{13}
	D*/J*	2.13×10^{14}	2.70×10^{14}	3.36×10^{14}	9.40×10^{12}	1.19×10^{13}	1.48×10^{13}	1.31×10^{13}	1.66×10^{13}	2.07×10^{13}
	E/K	4.27×10^{14}	4.91×10^{14}	5.73×10^{14}	1.86×10^{13}	2.13×10^{13}	2.49×10^{13}	5.53×10^{12}	6.36×10^{12}	7.41×10^{12}
	F/L	2.31×10^{15}	2.10×10^{15}	1.85×10^{15}	7.21×10^{12}	6.56×10^{12}	5.79×10^{12}			

Table S5 Attempt Frequency of the various hops in Hz as a function of pressure

	0 GPa	5	10
Hops from M1 Site			
G	3.22	3.05	2.88
H	3.16	3.27	3.38
I	0.59	0.28	0.01
I*	1.35	0.99	0.63
J	0.56	0.39	0.21
J*	1.29	0.81	0.32
Hops from I2 site			
I	0.39	0.29	0.17
I*	1.15	1.00	0.84
J	0.36	0.36	0.36
J*	1.09	0.78	0.47
K	1.08	1.42	1.78

Table S6: Variation in Activation Energy (in eV) of interstitial hops with pressure.

		[100]	[010]	[001]
Anhydrous vacancy	1000 K	3.92×10^{-14}	1.6×10^{-13}	1.88×10^{-10}
	1300	9.96×10^{-12}	3.00×10^{-11}	1.27×10^{-09}
	1600	3.30×10^{-10}	8.68×10^{-10}	5.30×10^{-09}
Hydrous vacancy	1000	7.78×10^{-22}	3.65×10^{-18}	2.48×10^{-08}
	1300	7.95×10^{-20}	3.73×10^{-16}	6.09×10^{-07}
	1600	2.98×10^{-13}	1.38×10^{-12}	5.23×10^{-06}
Interstitial	1000	2.94×10^{-12}	1.16×10^{-11}	6.13×10^{-12}
	1300	7.48×10^{-12}	2.87×10^{-11}	1.39×10^{-11}
	1600	1.53×10^{-11}	5.55×10^{-11}	2.46×10^{-11}

Table S7- Diffusion coefficients (m^2/s) of vacancies and interstitials in three directions at 5 GPa

		[100]	[010]	[001]
Anhydrous vacancy	1000 K	7.95×10^{-14}	2.11×10^{-13}	1.88×10^{-10}
	1300	1.72×10^{-11}	4.16×10^{-11}	1.19×10^{-09}
	1600	4.86×10^{-10}	1.07×10^{-09}	4.93×10^{-09}
Hydrous vacancy	1000	8.77×10^{-23}	4.11×10^{-19}	3.37×10^{-08}
	1300	1.27×10^{-20}	5.94×10^{-17}	8.32×10^{-07}
	1600	3.52×10^{-19}	1.65×10^{-15}	6.09×10^{-06}
Interstitial	1000	2.04×10^{-11}	9.05×10^{-11}	6.66×10^{-11}
	1300	3.66×10^{-11}	1.49×10^{-10}	8.44×10^{-11}
	1600	5.87×10^{-11}	2.18×10^{-10}	1.01×10^{-10}

Table S8- Diffusion coefficients (m^2/s) of vacancies and interstitials in three directions at 10 GPa

		0 GPa			5 GPa			10 GPa		
		[100]	[010]	[001]	[100]	[010]	[001]	[100]	[010]	[001]
Anhydrous Vacancy	1000 K	6.28×10^{-27}	3.20×10^{-26}	7.76×10^{-23}	1.20×10^{-28}	5.01×10^{-28}	5.76×10^{-25}	7.33×10^{-30}	1.95×10^{-29}	1.73×10^{-26}
	1300	2.87×10^{-21}	1.21×10^{-20}	1.26×10^{-18}	8.78×10^{-23}	2.64×10^{-22}	1.12×10^{-20}	1.62×10^{-23}	3.90×10^{-23}	1.11×10^{-21}
	1600	8.78×10^{-18}	3.86×10^{-17}	5.48×10^{-16}	7.07×10^{-19}	1.86×10^{-18}	1.13×10^{-17}	1.40×10^{-19}	3.08×10^{-19}	1.42×10^{-18}
Interstitial	1000	1.43×10^{-25}	3.13×10^{-25}	1.10×10^{-25}	8.98×10^{-27}	3.55×10^{-26}	1.87×10^{-26}	1.88×10^{-27}	8.35×10^{-27}	6.14×10^{-27}
	1300	1.19×10^{-21}	3.08×10^{-21}	1.01×10^{-21}	6.59×10^{-23}	2.53×10^{-22}	1.22×10^{-22}	3.43×10^{-23}	1.40×10^{-22}	7.91×10^{-23}
	1600	3.68×10^{-19}	7.54×10^{-19}	3.80×10^{-19}	3.28×10^{-20}	1.19×10^{-19}	5.27×10^{-20}	1.70×10^{-20}	6.31×10^{-20}	2.91×10^{-20}
Combined	1000	1.50×10^{-25}	3.45×10^{-25}	7.77×10^{-23}	9.10×10^{-27}	3.60×10^{-26}	5.94×10^{-25}	1.89×10^{-27}	8.37×10^{-27}	2.35×10^{-26}
	1300	4.06×10^{-21}	1.51×10^{-20}	1.26×10^{-18}	1.54×10^{-22}	5.17×10^{-22}	1.13×10^{-20}	5.04×10^{-23}	1.79×10^{-22}	1.19×10^{-21}
	1600	9.14×10^{-18}	3.93×10^{-17}	5.48×10^{-16}	7.39×10^{-19}	1.98×10^{-18}	1.14×10^{-17}	1.57×10^{-19}	3.71×10^{-19}	1.45×10^{-18}

Table S9- Diffusion rates (m^2/s) of anhydrous vacancies, interstitials and their combined diffusion rate at various pressures and temperatures for anhydrous forsterite.

	0 Gpa			5 Gpa			10 Gpa		
	[100]	[010]	[001]	[100]	[010]	[001]	[100]	[010]	[001]
	10 wt % ppm								
1000 K	2.69×10^{-25}	3.41×10^{-21}	1.34×10^{-12}	6.99×10^{-26}	2.85×10^{-22}	1.94×10^{-12}	8.74×10^{-27}	3.21×10^{-23}	2.64×10^{-12}
1300	4.10×10^{-21}	2.31×10^{-19}	3.58×10^{-11}	1.60×10^{-22}	2.96×10^{-20}	4.75×10^{-11}	5.14×10^{-23}	4.82×10^{-21}	6.49×10^{-11}
1600	1.57×10^{-16}	7.21×10^{-16}	2.65×10^{-10}	2.40×10^{-17}	1.10×10^{-16}	4.09×10^{-10}	1.57×10^{-19}	5.00×10^{-19}	4.76×10^{-10}
	100 wt % ppm								
1000 K	1.34×10^{-24}	3.41×10^{-20}	1.34×10^{-11}	6.17×10^{-25}	2.85×10^{-21}	1.94×10^{-11}	7.04×10^{-26}	3.21×10^{-22}	2.64×10^{-11}
1300	4.52×10^{-21}	2.17×10^{-18}	3.58×10^{-10}	2.16×10^{-22}	2.92×10^{-19}	4.75×10^{-10}	6.03×10^{-23}	4.66×10^{-20}	6.49×10^{-10}
1600	1.48×10^{-15}	6.86×10^{-15}	2.65×10^{-09}	2.34×10^{-16}	1.08×10^{-15}	4.09×10^{-09}	1.58×10^{-19}	1.66×10^{-18}	4.76×10^{-09}
	1000 wt % ppm								
1000 K	1.21×10^{-23}	3.41×10^{-19}	1.34×10^{-10}	6.09×10^{-24}	2.85×10^{-20}	1.94×10^{-10}	6.87×10^{-25}	3.21×10^{-21}	2.64×10^{-10}
1300	8.67×10^{-21}	2.16×10^{-17}	3.58×10^{-09}	7.75×10^{-22}	2.91×10^{-18}	4.75×10^{-09}	1.49×10^{-22}	4.64×10^{-19}	6.49×10^{-09}
1600	1.47×10^{-14}	6.82×10^{-14}	2.65×10^{-08}	2.33×10^{-15}	1.08×10^{-14}	4.09×10^{-08}	1.60×10^{-19}	1.33×10^{-17}	4.76×10^{-08}

Table S10- Diffusion rate of hydrous forsterite (combined anhydrous vacancy, interstitial and hydrous vacancy diffusion) at various pressures and temperatures with fixed water concentrations at γ=1.

	0 Gpa			5 Gpa			10 Gpa		
	[100]	[010]	[001]	[100]	[010]	[001]	[100]	[010]	[001]
	10 wt % ppm								
1000 K	1.50×10^{-25}	3.45×10^{-25}	3.59×10^{-20}	9.10×10^{-27}	3.60×10^{-26}	5.17×10^{-20}	1.89×10^{-27}	8.37×10^{-27}	7.03×10^{-20}
1300	4.06×10^{-21}	1.51×10^{-20}	5.47×10^{-17}	1.54×10^{-22}	5.17×10^{-22}	7.10×10^{-17}	5.04×10^{-23}	1.79×10^{-22}	9.69×10^{-17}
1600	9.15×10^{-18}	3.93×10^{-17}	5.45×10^{-15}	7.40×10^{-19}	1.98×10^{-18}	7.56×10^{-15}	1.57×10^{-19}	3.71×10^{-19}	8.79×10^{-15}
	100 wt % ppm								
1000 K	1.50×10^{-25}	3.46×10^{-25}	3.59×10^{-19}	9.10×10^{-27}	3.61×10^{-26}	5.17×10^{-19}	1.89×10^{-27}	8.38×10^{-27}	7.03×10^{-19}
1300	4.06×10^{-21}	1.51×10^{-20}	5.36×10^{-16}	1.54×10^{-22}	5.18×10^{-22}	7.10×10^{-16}	5.04×10^{-23}	1.79×10^{-22}	9.69×10^{-16}
1600	9.17×10^{-18}	3.94×10^{-17}	4.95×10^{-14}	7.44×10^{-19}	2.00×10^{-18}	7.55×10^{-14}	1.57×10^{-19}	3.71×10^{-19}	8.79×10^{-14}
	1000 wt % ppm								
1000 K	1.50×10^{-25}	3.54×10^{-25}	3.59×10^{-18}	9.10×10^{-27}	3.67×10^{-26}	5.17×10^{-18}	1.89×10^{-27}	8.46×10^{-27}	7.03×10^{-18}
1300	4.06×10^{-21}	1.52×10^{-20}	5.34×10^{-15}	1.54×10^{-22}	5.22×10^{-22}	7.10×10^{-15}	5.04×10^{-23}	1.80×10^{-22}	9.69×10^{-15}
1600	9.42×10^{-18}	4.06×10^{-17}	4.90×10^{-13}	7.82×10^{-19}	2.18×10^{-18}	7.55×10^{-13}	1.57×10^{-19}	3.72×10^{-19}	8.79×10^{-13}

Table S11- Diffusion rates (m^2/s) of hydrous forsterite (combined anhydrous vacancy, interstitial and hydrous vacancy diffusion) at various pressures and temperatures with fixed water concentrations at γ set to reflect an energy difference of -169 kJ/mol for R2.

11

	Atoms		
	q_{core} (eV)	q_{shell} (eV)	
Mg	2.0	n/a	
Si	4.0	n/a	
O	0.84819	-2.84819	
O_H	-1.426	n/a	
H	0.426	n/a	
	Buckingham Potential		
	A (eV)	ρ (Å)	C_{ij} (eV*Å^6)
Mg-O	1428.5	0.29435	0
Mg-O_H	1060.5	0.29435	0
Si-O	1283.907	0.32052	10.66158
Si-O_H	983.556	0.32052	10.66128
O^*-O^*	22764	0.149	27.88
O^*-H^b	311.96	0.25	0
	Morse		
	D_e (eV)	A (Å^{-1})	r_0 (Å)
H-OH	7.02525	2.03	0.9485
	Three Body		
	k3 (eV rad^{-2})	Θ_0(°)	
O^*-Si-O^*	2.0972	109.47	
	Spring		
	k2 (eV Å^{-2})		
O_{core}-O_{shell}	74.92038		

12 Table S12 Potentials used in our forcefields calculations. O (the normal oxygen in the crystal lattice) and O_H (the oxygen in a hydroxyl group) have some
13 unique but also some shared forcefields- O* represents both O and O_H. The Morse potential for O_H-H interactions was set to operate between 0 and 1.5 Å
14 whereas the Buckingham potential for O-H interactions was set to operate between 1.5-10 Å. This ensures (with a sensible starting geometry) that the O-H
15 bond is modelled by a Morse potential but the interaction of the oxygen in the OH group with the other Hydrogen in the vacancy is modelled with a

16 Buckingham potential. If both potentials are set to operate from 0- 10 Å then the hydrogen atoms either fall outside of the vacancy or into the centre of
17 the vacancy (depending upon starting geometry) which does not match the more accurate predictions of DFT.

18